SATELLITE EPHEMERIS CORRECTION VIA REMOTE SITE OBSERVATION FOR STAR TRACKER NAVIGATION PERFORMANCE IMPROVEMENT

THESIS

Capt Jorge E. Díaz

AFIT-ENG-MS-16-M-013

DEPARTMENT OF THE AIR FORCE
AIR UNIVERSITY

AIR FORCE INSTITUTE OF TECHNOLOGY

Wright-Patterson Air Force Base, Ohio

AFIT-ENG-MS-16-M-013

SATELLITE EPHEMERIS CORRECTION VIA REMOTE SITE OBSERVATION FOR STAR TRACKER NAVIGATION PERFORMANCE IMPROVEMENT

THESIS

Presented to the Faculty
Department of Electrical and Computer Engineering
Graduate School of Engineering and Management
Air Force Institute of Technology
Air University
Air Education and Training Command
in Partial Fulfillment of the Requirements for the
Degree of Master of Science in Electrical Engineering

Capt Jorge E. Díaz, B.S.E.E.

March 2016

DISTRIBUTION STATEMENT A
APPROVED FOR PUBLIC RELEASE; DISTRIBUTION UNLIMITED.

AFIT-ENG-MS-16-M-013

SATELLITE EPHEMERIS CORRECTION VIA REMOTE SITE OBSERVATION FOR STAR TRACKER NAVIGATION PERFORMANCE IMPROVEMENT

THESIS

Capt Jorge E. Díaz, B.S.E.E.

Committee Membership:

Maj Scott J. Pierce, PhD
Chair

John F. Raquet, PhD
Member

Richard G. Cobb, PhD
Member

AFIT-ENG-MS-16-M-013

Abstract

In order for celestial navigation observing satellites to provide accurate positioning estimates, precise ephemerides of the observed satellites are necessary. This work analyzed a method to correct for satellite ephemeris to be used in celestial navigation applications. This correction is the measured angle differences between the expected location of the satellite, which is given by propagating publicly available Two-Line Elements (TLE), and their observed angles from a precisely known reference site. Therefore, the angle difference can be attributed completely to satellite ephemeris error assuming instrument error was accounted for. The intent is to calculate this correction from the reference site and relate it to remote sites that have visibility of the same satellite, but where its own location is known with some uncertainty. The effects of increased baseline distances from the reference site, in addition to time delays when the correction was calculated are studied.

Satellite observations were simulated and propagated using TLEs. This simulated data was manipulated to calculate the angle difference and transform that angle to the viewpoint of the remote sites. This corrected observed angle was integrated using an extended Kalman Filter (EKF) with an inertial measurement unit (IMU) and a barometric altimeter. The performance of the position solution in the navigation filter was calculated as the error from simulated truth.

The satellite ephemeris error measured at a reference location becomes less observable by a remote user according to the line-of-sight transformation due to the reference-satellite-remote geometry. A mathematical formula for calculating the applicability of projecting the remote site observation to other locations is developed and compared to simulated ephemeris errors. This formula allows a user to define geographic regions of validity through ephemeris error tolerance. Estimating the ephemeris error with regular updates from a reference site resulted in a reduction of inertial measurement unit (IMU) drift and reducing the distance root mean squared (DRMS) error by a maximum of 98% under certain conditions.

AFIT-ENG-MS-16-M-013

To my wife, daughter and son.

Acknowledgements

I would like to thank my advisor, Maj Pierce, for his guidance, support and mentoring throughout this process. I also want to express my gratitude to Dr. Raquet and Dr. Cobb, my thesis committee members, for sharing their advice and expertise that helped keep me on track and fine tune this work. Special thanks to the great ANT center staff for providing the equipment, technical assistance, and admin support needed during this research.

I would also like to extend my thanks to my friends and mentors from my previous unit at Patrick AFB, since it was there where they encouraged and motivated me to pursue my graduate degree here at AFIT. Finally, I wish to thank my family, especially my wife for her support and constant encouragement during these last 18 months. Without their support, none of the work presented in this thesis would have been possible.

Capt Jorge E. Díaz

Table of Contents

Page

List of Abbreviations

LOP line of position

RA right ascension

DEC declination

COTS Commercial off-the-shelf

AFRL Air Force Research Laboratory

CCD charged-coupled device

LEO low-Earth orbit

SSN Space Surveillance Network

RSO resident space object

JSpOC Joint Space Operations Center

TLE Two-Line Element sets

FOV field of view

SGP4 Simplified General Perturbations-4

STK System Tool Kit

GPS Global Positioning System

COM Component Object Model

GNSS Global Navigation Satellite System

IMU inertial measurement unit

EKF extended Kalman filter

DoD Department of Defense

INS Inertial Navigation System

FOGM first-order Gauss Markov

ECEF Earth-Centered, Earth-Fixed

NED North-East-Down

DCM direction cosine matrix

AWGN additive white Gaussian noise

ANT Autonomy & Navigation Technology

ICD interface control document

SPIDER Sensor Processing for Inertial Dynamics Error Reduction

AFIT Air Force Institute of Technology

DRMS distance root mean squared

RMS root mean squared

GCRF Geocentric Celestial Reference Frame

List of Figures

List of Tables

SATELLITE EPHEMERIS CORRECTION VIA REMOTE SITE OBSERVATION
FOR STAR TRACKER NAVIGATION PERFORMANCE IMPROVEMENT

I. Introduction

In a world heavily dependent on Global Navigation Satellite System (GNSS), predominantly Global Positioning System (GPS), the navigation community has been actively exploring new methods of navigation to use where and when GPS is degraded. The Department of Defense (DoD) also has an interest in finding alternatives for navigating in GPS denied or degraded environments as directed by the National Space Policy of 2010. President Obama's National Space Policy of 2010 states, "Invest in domestic capabilities and support international activities to detect, mitigate, and increase resiliency to harmful interference to GPS, and identify and implement, as necessary and appropriate, redundant and back-up systems or approaches for critical infrastructure, key resources, and mission-essential functions."[16].

Celestial navigation is a viable option when operating in GPS degraded environments, especially when imaging illuminated satellites. Combining stars and a passing satellite in the same image, a line of position (LOP) can be calculated using the precise cataloged position of stars and resident space object (RSO) ephemeris [8]. In order for this method to provide accurate positioning estimates, precise ephemerides of the observed satellites are necessary. A clear advantage of celestial navigation is that stars are not jammable, and with GPS and communications satellite constellations, there is always a satellite visible. For example, the Iridium satellite constellation which resides in low-Earth orbit (LEO), consist of 6 orbital planes with 11 active satellites in each plane. These 66 active satellites provide coverage over the entire

Earth's surface at every moment.

This thesis focuses on a particular mathematical method of correcting ephemeris error by imaging a known RSO from a reference site, measuring the angle difference when compared to its expected location, and projecting that difference to remote sites for correction. The effects of applying this correction at different time epochs and at different baseline distances from the remote site are the primary focus of our work. The work performed does not include the image processing techniques to obtain those angles, that has been explained and demonstrated in [13], [22] and [11]. There are limitations to the RSO that can be imaged based on the RSO magnitude and sensor selection. During this research it was assumed the observations were made and the pointing angles to the RSO were extracted from the images.

1.1 Objective

When estimating an observer's position in celestial navigation by imaging satellites, inaccurate satellite ephemeris is the primary cause of error [19]. For this reason, this research intended to determine the performance improvement of an Inertial Navigation System (INS) coupled with a star tracker when correcting for the observed RSO ephemeris via observation from a reference site. This correction is intended for a regional geographical area near the reference site and with a relatively short time of relevance. The reason for this geographical and time restriction is because the entire orbit of the RSO is not corrected (i.e. velocity and other data is not determined). Instead the position of the RSO at a specific time epoch is corrected.

1.2 Assumptions and Applicability

This work assumes Two-Line Element sets (TLE) are publicly available for the observed RSOs. In addition to having acTLEs available to make the observations, the right ascension (RA) and declination (DEC) angles to the RSO are assumed to be previously extracted via image processing techniques. Errors from the image processing techniques to include the star catalog errors, were determined not to be a significant factor in our work since sensor noise was added. Additionally, time delays were introduced when analyzing the transformation matrix, but this delay does not account for system time errors. The TLE error introduced in this work is limited to an initial bias of ±0.005° in inclination and the right ascension of the ascending node values. This error remains constant throughout the different scenarios simulated.

This method of correcting for the ephemeris from a differential site first proposed by Pierce [19], could be used with RSOs with prior knowledge of its position and bright enough to be imaged with Commercial off-the-shelf (COTS) hardware. Prior knowledge of the RSO being imaged is a limiting factor in this method because the main idea is to measure the angle difference between the RSO's expected location and its observed location . However, the theory presented in this thesis should also be applicable to dimmer objects imaged by specialized equipment given its expected position.

1.3 Thesis Overview

Chapter II of this document describes previous related research which our work leverages. Chapter III details the modeling approach taken in our research and develops the dynamics and measurement models of the star tracker, along with the algorithms used to calculate navigation estimates. Chapter IV describes and analyzes the performance of the navigation states estimation using the proposed method of correcting for RSO ephemeris in simulated scenarios. Chapter V explains conclusions drawn from the results obtained in this research, presents possible applications and additional work of interest on this topic.

Appendix A derives the linearized measurement equations for the star tracker as applied to the position error states in the extended Kalman filter (EKF).

II. Background

This chapter describes the current approaches to using star trackers for positioning and background topics relevant to the further development of this correction approach.

An overview and method of solving for position using angles only measurements is provided in Section 2.1. Section 2.2 reviews the coordinate frame used in this research. Techniques describing how to make measurements to passing satellites using star trackers are presented in Section 2.3. Section 2.4 introduces the technique this research relies on to correct for satellite ephemeris error. Finally, Section 2.5 describes the algorithm used to incorporate star tracker measurements and estimate the navigation states.

2.1 Angles Only Navigation

The method of obtaining a fixed observer's position from a known observed object is a geometric problem that has been solved previously [3], [8], [9]. With one observation only, a LOP can be determined and the observer must lie somewhere on that line. However, with at least two observations the location where those LOP intersect will be the observer's position. The vector to the observed object as well as the object's coordinates have some error directly affecting the observer's position estimation. A visual representation of these measurements and the errors associated with one observation is depicted in Figure 1.

Kaplan presented a closed-formed solution for a fixed observer taking one or various n simultaneous observations used for triangulation and derived a generalized algorithm where the observer's position is time-dependent [9]. The term β_i is introduced to account for the curvature of the Earth. This term is important when the observations are made on, or near the surface of the Earth, and separated over large

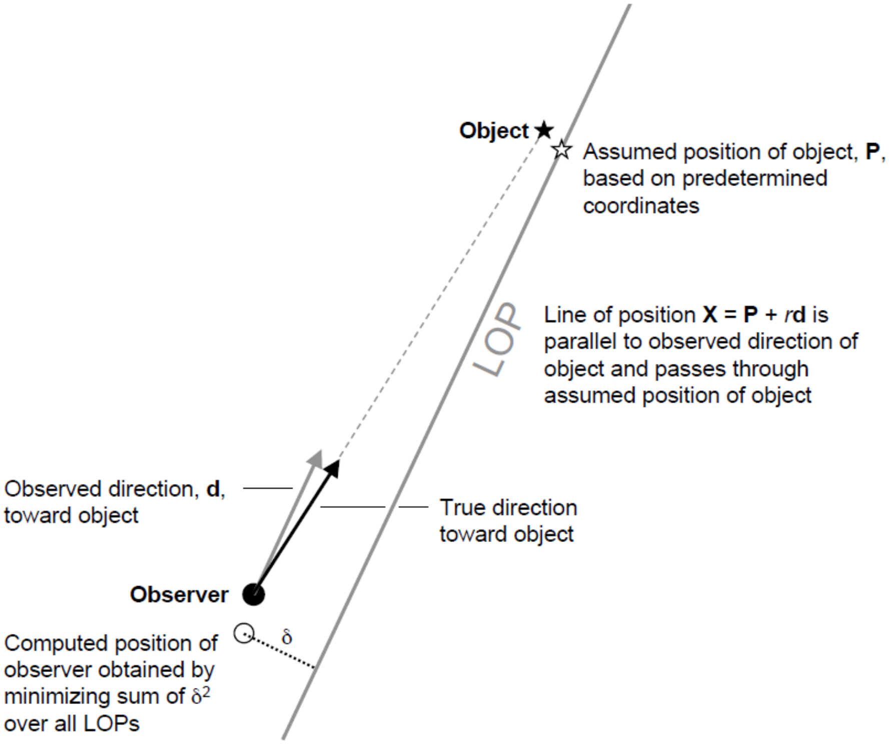

Figure 1. Geometry of a single observation. Both the observed direction of the object and the object's coordinates are assumed to have some error[9]

distances (tens of kilometers). The observer's position **X** and velocity vector **V** can be calculated using this algorithm, given the known position of the observed object **P**, and the unit vector **d** of the object from the observer. It is important to ensure the observed object's coordinates **P** and the unit vector of the observation **d** to be in the same reference frame. The resulting solution for the observer's position and velocity vector will be expressed in that particular reference frame. For the intended application in this thesis, the observer position will not be limited to a fixed location and the observations are not separated over large distances.

The work presented by Kaplan involves triangulation, which requires a sequence of angles-only measurements. In his paper, he introduced the idea of imaging satellites against a star background taking advantage of their finite slant range [9]. However, in this thesis the method does not involve triangulation because an accurate LOP can be obtained by using image processing techniques to extract pointing angles and precise ephemerides from the satellites.

2.2 Coordinate Systems

As presented in the previous section it is necessary to have the observations and the position of the observed objects in a common coordinate system. However, ultimately we're interested in representing position, velocity and attitude in the local level frame. he location of celestial objects are given by RA and DEC in the celestial sphere. The Geocentric Celestial Reference Frame (GCRF) is the standard geocentric frame that measures the RA east in the plane of the equator from the vernal equinox Υ. DEC angles northward from the equator are positive and angles southward are negative. Figure 2 depicts the celestial sphere and the references used for measuring RA and DEC. However, when observing objects orbiting near Earth a distinction must be

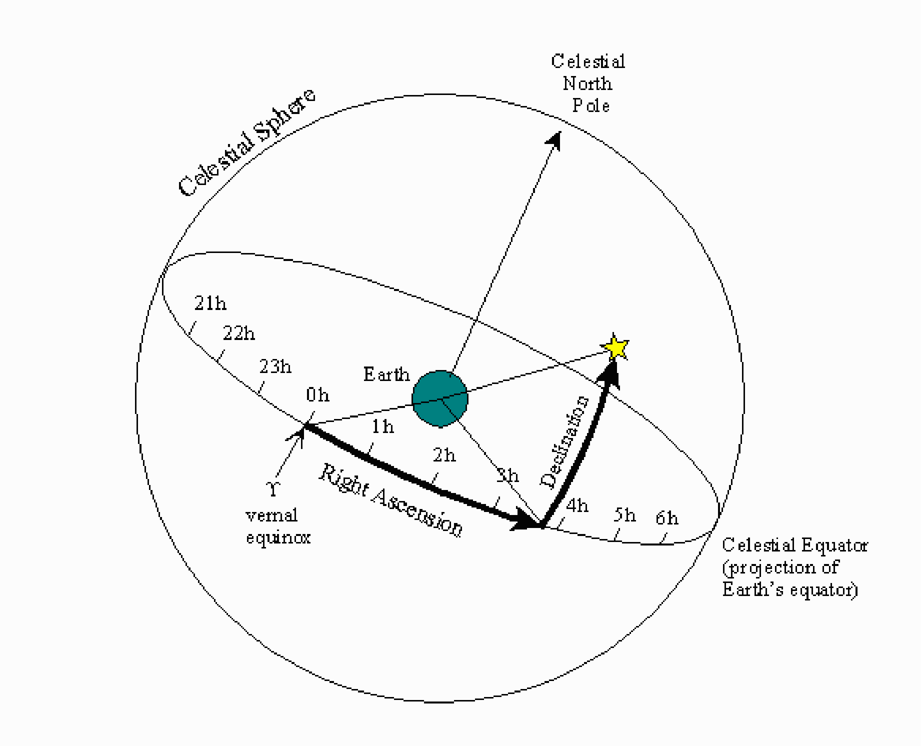

Figure 2. Right ascension (α) and declination (δ) in the celestial sphere[6]

made between geocentric and topocentric angles. Geocentric is referred to frame systems which the origin is at the center of the earth. Topocentric, on the other hand, are those that the origin is on or near the surface of the Earth. For distant celestial objects, like stars, the difference between geocentric and topocentric are negligible because those objects appear to be in the same direction anywhere from Earth, but that is not the case for near-Earth objects. For topocentric observations it is important to know the origin of the observation [25] and time of the observations. These two parameters are important to know when converting from topocentric to geocentric, and vice versa. In this research the angle measurements received from the star tracker are topocentric.

Similar to the GCRF, the Earth-Centered, Earth-Fixed (ECEF) frame has its origin at the center of the Earth. However, this frame is fixed to the rotating Earth with the first axis in the direction of the Prime Meridian, the second axis orthogonal to the first and within the equatorial plane, and the third axis in the direction of the North pole orthogonal to the equatorial plane. Typically, location in the ECEF are expressed as $[x, y, z]$ vectors.

2.3 Observations

Over the past decade there have been several publication [11, 20, 22], demonstrating the capability of COTS telescopes and charged-coupled device (CCD) sensors, used to obtain high accuracy angular observations of space objects. The Raven program [22] developed by the Air Force Research Laboratory (AFRL), demonstrated this capability by using COTS hardware and software to track, image and obtain accurate angular observations of space objects with a standard deviation of approximately one arcsecond. The advantage of using COTS hardware and software is the reduction in cost, schedule and the flexibility to change the system configuration based on particular requirements. These Raven-class systems have been used to collect astrometric and photometric data on LEO satellites, to include 1 kg picosatellites [11]. Primarily, these Raven-class systems have been used to support the Space Surveillance Network (SSN) to track and estimate the orbit of RSO, but in this thesis the primary goal is to obtain astrometric data of the RSO at a given time and not to estimate its entire orbit.

These astrometric data which are precise positions of objects in the celestial sphere, are obtained by processing images of satellites in a background of precisely known stars [2]. The open source package *Astrometry.net* [12] processes astronomical images and provides astrometric data. The authors claim a success rate above 99.9% with no false positive [12]. The output obtained from *Astrometry.net* is used to convert from pixel coordinates in the images to topocentric RA DEC in the celestial sphere. With this data it is now possible to estimate the satellite's position in the celestial sphere.

Levesque [13] presented a technique to obtain this RA DEC measurement of satellite streaks by processing astronomical images and using a software package similar to *Astrometry.net*. His detection algorithm consisted of removing the background from the image through an iterative process, removing stars and finally identifying the streak by convolving the expected streak with the remaining objects in the image. The algorithm detection rate is dependent on both the brightness and the length of the streak. Another algorithm to automatically detect LEO object streaks is developed by Oniga [17]. Oniga's method differs from Levesque primarily in how the background is removed. The algorithm presented removes most stars as part of the background removal process, claiming their method is less complex than Levesque's algorithm. The results from these image processing techniques, is to obtain pointing vectors to the RSO from the observer's position. This data extracted from the images in combination with other data from the RSO (i.e. ephemeris), is possible to determine the observer's position using Kaplan's algorithm [9] presented earlier in Equation (**??**).

More than 16,000 RSO are tracked by the Joint Space Operations Center (JSpOC)[5] where only around 5% are functioning payload or satellites. The JSpOC collects between 380,000 to 420,000 observations per day. Using these observations, positions and velocities of RSOs are updated, and these updates are published in the form of TLE [25]. Implementing a simplified perturbations model like the Simplified General Perturbations-4 (SGP4)[7] in System Tool Kit (STK)[23], an observation window can be determined using TLE for the object of interest. It is important that the RSO's expected error in position is within the star tracker field of view (FOV) at both the reference site and remote site to ensure the RSO is within the image frame. For example, for a star tracker with a FOV of 1° observing an RSO at 1000 km, the image frame will cover approximately 13.9 km. If the RSO travels around 6 km/sec, the object will be in the frame for approximately 2 seconds.

Therefore, in order to capture the RSO in the image, precise time must be used. Synchronizing the computer clock with the telescope GPS receiver should provide enough precision to capture the RSO in the frame [20], given the telescope was pointing in the right direction. At least the same time precision must be used to tag the images. Time tagging the images is crucial in order to determine the RSO's position and velocity when using Levesque's [13] or Oniga's [17] processing methods.

The work presented in this thesis does not include any image processing techniques to extract pointing angles to the RSO. In this work it was assumed that these pointing angles are available, previously extracted from images using a similar technique or one of the methods presented in this section.

2.4 Differential Site Ephemeris Correction

When determining position using RSO observations against a star background, it is important to precisely know the RSO's position. As showed previously in **??**, the accuracy of this data has a direct impact in the calculated observer's position. In this thesis the position of the RSO is determined using publicly available TLE and propagating forward in time to the desired time epoch using SGP4 in STK. Typically, TLE propagated using SGP4 for RSOs in LEO experience a positional error rate of approximately, 1.5 km/day [14]. This positional error theoretically can be removed by making observations from a reference site with known position. With the reference site's known position and an estimation of the RSO's range, a position estimate of the RSO can be calculated. This approach assumes all other sources of error are accounted for and any difference in the measurements is a direct result of the RSO positional error. Pierce presented a method [19] for calculating this angle difference called $\boldsymbol{\Delta}\theta$, and to project it from the reference site to the remote observer's frame. The idea is that the observer can apply this projected difference to the observed measurements and correct for the RSO's position, improving the accuracy of its position estimate.

The equations presented in [19] for projecting the measured angle difference from the expected are presented below in Equations (2.1) to (2.12). The angle difference from the expected to the truth (observed) is calculated at the reference site represented by $\boldsymbol{\Delta}\theta$ in Equation (2.1). This residual is calculated in radians and can be converted to meters by multiplying the expected slant range ρ_d in meters as depicted in Equation (2.2)[19].

$$\boldsymbol{\Delta\theta} = \begin{bmatrix} \Delta\alpha \\ \Delta\delta \end{bmatrix} = \begin{bmatrix} \alpha_{truth} - \alpha_{expected} \\ \delta_{truth} - \delta_{expected} \end{bmatrix} \tag{2.1}$$

where, $\Delta\alpha$ is the RA residual given by the difference between truth α_{truth} and expected

$\alpha_{expected}$. Similarly, $\Delta\delta$ is the DEC residual given by the difference between truth δ_{truth} and expected $\delta_{expected}$.

$$\boldsymbol{\Delta\theta}_m = \boldsymbol{\Delta\theta} \cdot \rho_d = \begin{bmatrix} \Delta\alpha_m \\ \Delta\delta_m \end{bmatrix} \tag{2.2}$$

For the equations listed below, the estimated range is used because the scenario assumes the reference site does not have the capability to measure range to the RSO. Equation (2.3) represents the unit vector along the line of sight from the reference site to the RSO. The unit vector in the direction of the right ascension is calculated using Equation (2.7), and in the direction of declination is given by Equation (2.9)[19].

$$\mathbf{u}_{1d} = \frac{\mathbf{P}_d}{\rho_d} \tag{2.3}$$

where the pointing vector $\mathbf{P}$ from the differential site is defined by,

$$\mathbf{P} = \begin{bmatrix} P_x \\ P_y \\ P_z \end{bmatrix} = \begin{bmatrix} x_s - x_o \\ y_s - y_o \\ z_s - z_o \end{bmatrix} \tag{2.4}$$

and slant range ρ by,

$$\rho = \sqrt{P_x^2 + P_y^2 + P_z^2} \tag{2.5}$$

$$\mathbf{u}_{2temp} = \mathbf{u}_{1d} \times [0 \quad 0 \ -1]^T \tag{2.6}$$

$$\mathbf{u}_{2d} = \frac{\mathbf{u}_{2temp}}{\|\mathbf{u}_{2temp}\|} \tag{2.7}$$

$$\mathbf{u}_{3temp} = \mathbf{u}_{1d} \times \mathbf{u}_{2d} \tag{2.8}$$

$$\mathbf{u}_{3d} = \frac{\mathbf{u}_{3temp}}{\|\mathbf{u}_{3temp}\|} \tag{2.9}$$

These unit vectors from the reference site are multiplied by their respective angle residuals as showed in Equation (2.10). This projects the observation angle residuals from the reference site's image frame to the RA DEC frame [19].

$$\boldsymbol{\Delta\theta}_m^p = \Delta\alpha_m \cdot \mathbf{u}_{2d} + \Delta\delta_m \cdot \mathbf{u}_{3d} \tag{2.10}$$

$\boldsymbol{\Delta\theta}_m^p$ is used in Equation (2.11) by multiplying it with the unit vectors from the remote site to project the residual from the RA DEC frame to the remote site's image frame. The unit vectors for the remote $\mathbf{u}_o$ site are also calculated using Equations (2.3) to (2.9)[19].

$$\boldsymbol{\Delta\theta}_{m,o}^e = \begin{bmatrix} \Delta\alpha_{m,o}^e \\ \Delta\delta_{m,o}^e \end{bmatrix} = \begin{bmatrix} \boldsymbol{\Delta\theta}_m^p \cdot \mathbf{u}_{2o} \\ \boldsymbol{\Delta\theta}_m^p \cdot \mathbf{u}_{3o} \end{bmatrix} \tag{2.11}$$

To convert the projected residual to radians, $\boldsymbol{\Delta\theta}_{m,o}^e$ is divided by the expected slant range ρ_o from the remote site to the RSO as showed in Equation (2.12)[19].

$$\boldsymbol{\Delta\theta}_o = \frac{\boldsymbol{\Delta\theta}_{m,o}^e}{\rho_o} \tag{2.12}$$

Combining Equations (2.10) to (2.12) and rearranging these equations, yields Equation (2.13) which is the angle residual from the expected and observed angle at the reference site.

$$\boldsymbol{\Delta\theta}_o = \frac{\rho_d}{\rho_o} \begin{pmatrix} \Delta\alpha_d(\mathbf{u}_{2d} \cdot \mathbf{u}_{2o}) + \Delta\delta_d(\mathbf{u}_{3d} \cdot \mathbf{u}_{2o}) \\ \Delta\alpha_d(\mathbf{u}_{2d} \cdot \mathbf{u}_{3o}) + \Delta\delta_d(\mathbf{u}_{3d} \cdot \mathbf{u}_{3o}) \end{pmatrix} \tag{2.13a}$$

$$= \frac{\rho_d}{\rho_o} \begin{pmatrix} (\mathbf{u}_{2d} \cdot \mathbf{u}_{2o}) & (\mathbf{u}_{3d} \cdot \mathbf{u}_{2o}) \\ (\mathbf{u}_{2d} \cdot \mathbf{u}_{3o}) & (\mathbf{u}_{3d} \cdot \mathbf{u}_{3o}) \end{pmatrix} \begin{bmatrix} \Delta\alpha_d \\ \Delta\delta_d \end{bmatrix} \tag{2.13b}$$

From Equation (2.13), $\mathbf{W}$ is defined as the transformation matrix, which when left multiplied to the reference site's corrections projects it to the remote's image frame.

$$\mathbf{W} = \frac{\rho_d}{\rho_o} \begin{pmatrix} (\mathbf{u}_{2d} \cdot \mathbf{u}_{2o}) & (\mathbf{u}_{3d} \cdot \mathbf{u}_{2o}) \\ (\mathbf{u}_{2d} \cdot \mathbf{u}_{3o}) & (\mathbf{u}_{3d} \cdot \mathbf{u}_{3o}) \end{pmatrix} \tag{2.14}$$

With the correction $\boldsymbol{\Delta\theta}_o$ properly projected to the remote site, it can be applied to the remote's observations. Using the same Equations (2.3) to (2.9) the unit vectors from the remote site's image frame are calculated, in order to apply the correction from the reference site.

Various baseline distances and RSO orbits were simulated and evaluated in [19]. Further investigation to this method was recommended by Pierce in his dissertation [19] as a viable solution to correct for ephemeris error and improve position accuracy. This method of projecting angle residual from reference to remote site will be studied in this thesis. The focus of this work was on the effects of varying baseline distance of the remote site from the reference site and time delay between time of the observation and time of applying the residual correction at the remote site.

2.5 Navigation Estimation

Navigation state errors were estimated using an extended Kalman filter (EKF) which is a recursive data processing algorithm used when the dynamics or measurement models are non-linear. A key reason for its optimality is that Kalman filters incorporate all information that is made available [18]. The EKF uses the same two step process of propagate and update of the linear Kalman filter, and implements the same equations for those steps. The propagation step uses the dynamics and measurement model to propagate the state estimates and the state covariance matrix forward in time. Similarly, the update step updates the state estimates and covariance matrix whenever a measurement from the sensors is available. The Kalman filter equations use the state space representation. States are represented as an n-dimensional vector $\mathbf{x}$. The system dynamics are represented by $\mathbf{F}$, with control inputs $\mathbf{u}$ and dynamic driving noise $\mathbf{w}$. Measurements of those states are represented by $\mathbf{z}$, with measurement corruption noise $\mathbf{v}$.

2.5.1 State Model

For a linear system, the dynamic and measurement model are represented in state space by Equation (2.15) and Equation (2.16) [18].

$$\dot{\mathbf{x}}(t) = \mathbf{F}(t)\mathbf{x}(t) + \mathbf{B}(t)\mathbf{u}(t) + \mathbf{G}(t)\mathbf{w}(t) \tag{2.15}$$

$$\mathbf{z}(t) = \mathbf{H}(t)\mathbf{x}(t) + \mathbf{v}(t) \tag{2.16}$$

$\mathbf{B}$ and $\mathbf{G}$ in Equation (2.15) map the control input and dynamic noise to the states, respectively. $\mathbf{H}$ in Equation (2.16) is the measurements matrix. For systems with either non-linear dynamics or non-linear measurement models, the system is represented as follows [18].

$$\dot{\mathbf{x}}(t) = \mathbf{f}\left[\mathbf{x}(t), \mathbf{u}(t), t\right] + \mathbf{G}(t)\mathbf{w}(t) \tag{2.17}$$

$$\mathbf{z}(t_i) = \mathbf{h}\left[\mathbf{x}(t_i), t_i\right] + \mathbf{v}(t_i) \tag{2.18}$$

For both linear and non-linear systems, the dynamics and measurements noises are assumed to be zero-mean additive white and Gaussian with cross covariance matrices given by Equations (2.19) and (2.20), respectively.

$$E\{\mathbf{w}(t)\mathbf{w}(t+\tau)^T\} = \mathbf{Q}(t)\delta(\tau) \tag{2.19}$$

$$E\{\mathbf{v}(t_i)\mathbf{v}(t_j)^T\} = \mathbf{R}(t_i)\delta_{ij} \tag{2.20}$$

where $E\{\}$ is the expectation operator and $\delta(\tau)$ is a Dirac delta function.

In order to use the same linear Kalman filter equations, the non-linear equations describing the system were linearized about the state estimates using a first-order Taylor series expansion. Higher terms (non-linear) are neglected, leaving a linear approximation of the non-linear function.

2.5.2 Kalman Filter

As stated in the previous section, the Kalman filter consist of two main steps; propagation and update. For linear systems, the states are propagated forward by multiplying the states by the state transition matrix $\mathbf{\Phi}$ [18]

$$\mathbf{\Phi}(t_{i+1}, t_i) = e^{\mathbf{F}\Delta t} \tag{2.21}$$

where Δt is given by the time interval from t_i to t_{i+1}. Using the state transition matrix, the state estimates and the state cross covariance matrix are propagated forward in time with Equation (2.22) and Equation (2.23), respectively [18].

$$\hat{\mathbf{x}}(t_{i+1}^-) = \mathbf{\Phi}(t_i)\hat{\mathbf{x}}(t_i^+) \tag{2.22}$$

$$\mathbf{P}(t_{i+1}^-) = \mathbf{\Phi}(t_i)\mathbf{P}(t_i^+)\mathbf{\Phi}(t_i)^T + \mathbf{Q_d}_i \tag{2.23}$$

where $\mathbf{Q_d}_i$ is given by

$$\mathbf{Q_d}_i \triangleq \int_{ti}^{t_{i+1}} \mathbf{\Phi}(t_{i+1}, \tau)\mathbf{G}(\tau)\mathbf{Q}(\tau)\mathbf{G}(\tau)^T\mathbf{\Phi}(t_{i+1}, \tau)^T \mathrm{d}\tau \tag{2.24}$$

The non-linear matrix $\mathbf{f}(\cdot)$ and $\mathbf{h}(\cdot)$ are linearized by taking the Jacobian in order to use the linear Kalman filter equations to propagate and update the state estimates.

$$\mathbf{F}_i \triangleq \left.\frac{\partial \mathbf{f}[\mathbf{x}(t), \mathbf{u}(t), t]}{\partial \mathbf{x}(t)}\right|_{\mathbf{x}=\widehat{\mathbf{x}}(t_i^+)} \tag{2.25}$$

$$\mathbf{H}_{i+1} \triangleq \left.\frac{\partial \mathbf{h}[\mathbf{x}(t_i), t_i]}{\partial \mathbf{x}(t_i)}\right|_{\mathbf{x}=\widehat{\mathbf{x}}(t_{i+1}^-)} \tag{2.26}$$

With the linearized matrices calculated using Equations (2.25) and (2.26), the states and cross covariance matrix are propagated from t_i to t_{i+1}^- using Equations (2.22) and (2.23). Similarly the states and cross covariance matrix are updated from t_{i+1}^- to t_{i+1}^+ with the following equations [18].

$$\widehat{\mathbf{x}}(t_{i+1}^+) = \widehat{\mathbf{x}}(t_{i+1}^-) + \mathbf{K}(t_{i+1})[\mathbf{z}(t_{i+1}) - \mathbf{h}(\widehat{\mathbf{x}}(t_{i+1}^-), t_{i+1})] \tag{2.27}$$

$$\mathbf{P}(t_{i+1}^+) = [\mathbf{I} - \mathbf{K}(t_{i+1})\mathbf{H}(t_{i+1})]\mathbf{P}(t_{i+1}^-) \tag{2.28}$$

where **K** is the Kalman gain, defined by Equation (2.29) [18].

$$\mathbf{K}_{i+1} = \mathbf{P}(t_{i+1}^-)\mathbf{H}^T(t_{i+1}) \left[\mathbf{R}(t_{i+1}) + \mathbf{H}(t_{i+1})\mathbf{P}(t_{i+1}^-)\mathbf{H}^T(t_{i+1})\right]^{-1} \tag{2.29}$$

Maybeck [18] provides further detail and complete derivations of these equations for the linear Kalman filter as well as for the EKF.

2.6 Summary

This chapter described previous research relevant to the use of star tracker imaging of LEO passing satellites for navigation on Earth. Additionally, the reference frame used in this research is explained, along with the mathematical technique for correcting satellite ephemeris that is studied in this research. Finally, it introduced an overview of the Kalman filter algorithm, along with the equations used for the propagation and update steps.

III. Computer Modeling

3.1 Introduction

This chapter details the simulation setup and approach used to simulate and analyze the data. Section 3.2 describes how the ephemeris data was acquired, simulated and used for analysis. Sections 3.3 and 3.4, explain the process used for correcting satellite ephemeris when the remote and reference site have distance differences and delay by the time the correction is applied. Finally, Section 3.5 describes the dynamics and measurment models for sensors used by the EKF to estimate the navigation states.

3.2 Systems Took Kit (STK) Simulation

A scenario was created in STK [23] with the reference site given by the initial location of the remote site's trajectory plus the baseline distance specified in the scenario. The observations were made from this reference site to measure the angle difference between the expected and truth angles. The RSO's TLEs used in STK for the simulations were downloaded from CelesTrak [4]. To generate the difference between the expected and the observed angles, a bias was added to the TLE in the scenario. This bias was introduced in the form of a constant bias of $\pm 0.005°$ in the right ascending node and inclination to the TLE, which was then labeled as truth. This added bias in the TLE resulted approximately in 1 mili radians difference between the truth and expected RSO, which translates to approximately 1 km in distance at a range of 1000 km. This modification to the TLE was made using a text editor manually before importing it to STK. This resulted in two distinct objects in STK to generate separate data sets for analysis, one labeled as truth (i.e. TLE plus bias) and expected (i.e. TLE). A flow chart diagram of this process is depicted in

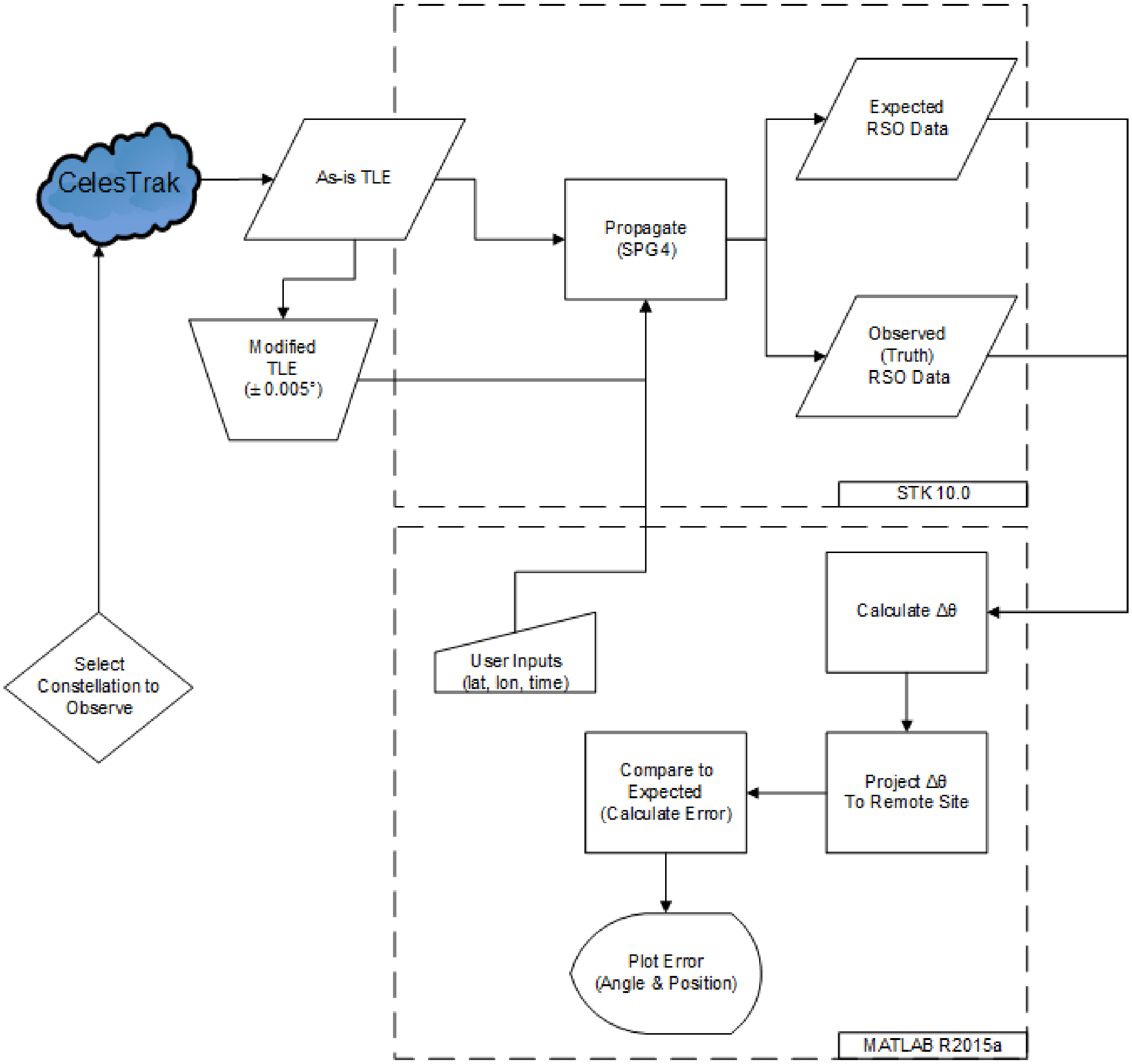

Figure 3. STK and MATLAB simulation flow chart.

Figure 3.

A minimum elevation angle of 10° above the horizon was set for the reference site as a constraint, to clear any possible line of sight obstruction. With the TLEs and reference loaded in the scenario, access from the site to the RSO was calculated using STK. This data can be extracted creating custom reports in STK and export the necessary data via comma separated value (.csv) files. In this research the data was extracted from STK via MATLAB®[15] by establishing a Component Object Model (COM) connection to STK. This method was preferred since all the calculations were performed in MATLAB® and to maximize process automation. The data extracted from STK to perform the calculations were the ECEF coordinates for both the expected and the truth positions. With the coordinates of the RSO and the observer's position, the pointing vector was calculated and transformed to topocentric RADEC using Vallado's *Algorithm 26* [25]. The algorithm uses Equation (3.1) for calculating the topocentric right ascension and Equation (3.2) for topocentric declination.

$$\alpha = \tan^{-1}\left(\frac{P_y}{P_x}\right) = \text{atan2}(P_y, P_x) \tag{3.1}$$

$$\delta = \sin^{-1}\left(\frac{P_z}{\rho}\right) \tag{3.2}$$

To calculate the unit vector of the observed RSO, the slant range is needed as showed in Equation (2.3). As simulated, neither the reference nor the remote site have the capability of measuring range to the RSO. Therefore, the slant range used for the observed calculations is the same as the range for the expected. An example calculation of the topocentric and unit vectors for the reference site are shown below.

Given an observer located at (6378.137, 0, 0) km and satellite passing overhead at (7368.084, 0, 383.91) km

$$\begin{aligned}
\rho = \sqrt{P_x^2 + P_y^2 + P_z^2} &= \sqrt{(x_{RSO} - x_{site})^2 + (y_{RSO} - y_{site})^2 + (z_{RSO} - z_{site})^2} \\
&= \sqrt{(989.947)^2 + (0)^2 + (383.91)^2} \\
&= 1061.782 \text{ km} \\
\alpha = \tan^{-1}&\left(\frac{0}{989.947}\right) = 0 \text{ rad} \\
\delta = \sin^{-1}&\left(\frac{383.91}{1061.782}\right) = 0.370 \text{ rad}
\end{aligned}$$

All the necessary data are available to calculate the pointing vector $\mathbf{P}_d$ and the corresponding unit vectors $\mathbf{u}_{1d}, \mathbf{u}_{2d}, \mathbf{u}_{3d}$.

$$\begin{aligned}
\mathbf{u}_{1d} &= \frac{\mathbf{P}_d}{\rho} = \frac{[989.947,\ 0,\ 383.91]}{1061.782} \\
&= [.932344,\ 0,\ 0.361571] \\
\mathbf{u}_{2d} &= \frac{\mathbf{u}_{1d} \times [0\ 0\ -1]^T}{|\mathbf{u}_{1d} \times [0\ 0\ -1]^T|} = [0,\ 0.93234,\ 0] \\
\mathbf{u}_{3d} &= \frac{\mathbf{u}_{1d} \times \mathbf{u}_{2d}}{|\mathbf{u}_{1d} \times \mathbf{u}_{3d}|} = [-0.33711,\ 0,\ 0.86926]
\end{aligned}$$

With the unit vectors calculated the angle difference $\boldsymbol{\Delta\theta}$ can be projected to the observer's frame and then with another site's unit vectors, project it to that site's image frame using Equations (2.10) to (2.12) and (2.13).

3.3 STK Baseline Distance Variant

Using the scenario constraints and following the same process presented in Section 3.2, the baseline distance from the reference to the remote site was increased in 50 km increments in a iterative process, to a maximum of 2000 km. 2000 km is approximately the radius of the access area for a RSO in LEO and a minimum elevation angle of 10°. In the simulations, the geodetic latitude and longitude of the remote site are calculated using the haversine equations [21].

The haversine equations provide great-circle distances between two locations assuming the Earth is a sphere. These equations were used to determine the latitude and longitude of the remote site given a baseline distance and bearing from the reference site. A MATLAB® function was created to calculate this new reference site location. The inputs required for this function are geodetic latitude and longitude in radians, bearing in degrees clockwise from North, and distance in meters. The outputs of this function are the geodetic latitude and longitude of the remote site in both radians and degrees. A sample MATLAB® call would be,

```
[lat2,lon2,lat2_d,lon2_d]= haversine(lat1,lon1,bearing,distance)
```

The haversine equations used in this function assume the Earth has radius of 6371 km. Using the haversine equations, latitude for the remote site is calculated using Equation (3.3) and longitude using Equation (3.4). In both these equations $\Delta = \frac{d}{R}$, where d is the baseline distance in meters from the reference to the remote site, R is the Earth radius and φ is the bearing in radians. Within the MATLAB® function the input bearing is converted to radians before being used in Equation (3.3) and Equation (3.4).

$$lat2 = \arcsin(\sin(lat1) \cdot \cos(\Delta) + \cos(lat1) \cdot \sin(\Delta) \cdot \cos(\varphi)) \tag{3.3}$$

$$lon2 = lon1 + \text{atan2}(\sin(\varphi) \cdot \sin(\Delta) \cdot \cos(lat1), \cos(\Delta) - \sin(lat1) \cdot \sin(lat2)) \tag{3.4}$$

This new geodetic latitude and longitude was used to calculate the topocentric RA DEC from STK for the remote site. This process of calculating latitude, longitude and obtaining line of sight measurements for the new remote site was repeated in MATLAB®. The objective was to analyze the accuracy of the transformation matrix **W** showed in Equation (2.14) with increased distances. Acquiring simulation data with this information will validate the Differential Site Ephemeris Correction method presented in Section 2.4, and provide performance information at different distances.

3.4 STK Time Variant

We followed a similar approach when analyzing the effects of time delay in the performance of the transformation matrix **W**. First, both the remote site and the reference site were co-located. With the two sites co-located the time delay was increased from 0 seconds to 30 seconds.

Basically, the time delay affects the transformation matrix by calculating $\mathbf{W}$ using an old (stale) angle correction $\Delta\boldsymbol{\theta}$ along with the reference site unit vectors associated with that $\Delta\boldsymbol{\theta}$. When the measurements received by the EKF are the reference site unit vectors and the angle correction $\Delta\boldsymbol{\theta}$. To calculate $\mathbf{W}$ the filter then uses the measured angles from the remote site. These old measurements coming from the reference site are used in combination with the reference site real-time measurements to calculate $\mathbf{W}$ using Equation (2.14). This accomplished the desired objective of calculating $\mathbf{W}$ using old (stale) angle corrections, and applying it at a current time.

The effects of combining these two variables (distance and time) in the position estimates are presented in the next chapter.

3.5 EKF Model

With the methodology presented in Section 3.3 for distance variant measurements and Section 3.4 for time variant, a model for incorporating these measurements in the EKF is presented in this section. The sensors integrated in the EKF are an IMU, a barometric altimeter and a star tracker. The dynamics and measurement models for these sensors are presented in this section. The EKF estimates the error states using a Pinson error model [24]. The Pinson error model provides the continuous-time dynamics equations for the IMU errors. This was augmented with altimeter and the star tracker dynamic and measurement models to completely describe our system.

3.5.1 IMU Model

IMU provides changes in velocity $\mathbf{\Delta v}$, and attitude $\mathbf{\Delta}\theta$, which when integrated over a time interval and provided the initial conditions, result in an estimate of velocity, position, attitude and heading. The IMU accelerometers are modeled to include a first-order Gauss Markov (FOGM) bias, $\mathbf{b}_a$, and additive white Gaussian noise (AWGN), $\mathbf{w}_a$, according to

$$\mathbf{\Delta v} = \mathbf{\Delta v}_{true} + \mathbf{b}_a + \mathbf{w}_a \tag{3.5}$$

where the bias and noise are uncorrelated as well as the noise inputs between each axis.

$$E[\mathbf{w}_a(t)\mathbf{w}_a(t+\tau)] = q_a\mathbf{I}_{3\times3}\delta(\tau) \tag{3.6}$$

$$E[\mathbf{w}_a(t)\mathbf{b}_a(t+\tau)] = \mathbf{0}_{3\times3} \tag{3.7}$$

The bias noise is modeled as

$$\dot{\mathbf{b}}_a(t) = -\frac{1}{\tau_a}\mathbf{b}_a(t) + \mathbf{w}_{b_a} \tag{3.8}$$

where τ_a is the time constant and $\mathbf{w}_{b_a}$, is AWGN with noise strength given by

$$E[\mathbf{w}_{b_a}(t)\mathbf{w}_{b_a}(t+\tau)] = \frac{2\sigma_a^2}{\tau_a}\mathbf{I}_{3\times3}\delta(\tau) \tag{3.9}$$

Similarly, the IMU gyroscopes are modeled to include FOGM bias, $\mathbf{b}_g$, and AWGN, $\mathbf{w}_g$, according to

$$\mathbf{\Delta}\boldsymbol{\theta} = \mathbf{\Delta}\boldsymbol{\theta}_{true} + \mathbf{b}_g + \mathbf{w}_g \tag{3.10}$$

where the bias and noise are uncorrelated as well as the noise inputs between each axis.

$$E[\mathbf{w}_g(t)\mathbf{w}_g(t+\tau)] = q_g\mathbf{I}_{3\times 3}\delta(\tau) \tag{3.11}$$

$$E[\mathbf{w}_g(t)\mathbf{b}_g(t+\tau)] = \mathbf{0}_{3\times 3} \tag{3.12}$$

Similar to the accelerometers, the gyroscopes' biases are modeled as

$$\dot{\mathbf{b}}_g(t) = -\frac{1}{\tau_g}\mathbf{b}_g(t) + \mathbf{w}_{b_g} \tag{3.13}$$

where τ_g is the time constant and $\mathbf{w}_{b_g}$, is AWGN with noise strength given by

$$E[\mathbf{w}_{b_g}(t)\mathbf{w}_{b_g}(t+\tau)] = \frac{2\sigma_g^2}{\tau_g}\mathbf{I}_{3\times 3}\delta(\tau) \tag{3.14}$$

With the model describing the IMU accelerometers and gyroscopes, the state vector used in the EKF can be defined. The first error states are the ones related to the information provided by the IMU.

$$\mathbf{x}_{INS} = [Lat,\ lon,\ h,\ v_N,\ v_E,\ v_D,\ \theta,\ \phi,\ \psi]^T \tag{3.15a}$$

$$\mathbf{x}_{INS} = [\mathbf{p}_{INS},\ \mathbf{v}_{INS},\ \boldsymbol{\theta}^{\tilde{n}}_{INS}]^T \tag{3.15b}$$

where, position $\mathbf{p}$ is given by geodetic latitude, longitude and altitude. Velocity $\mathbf{v}$ is defined as the velocity in the local level North-East-Down (NED) frame, relative to the Earth. Attitude $\boldsymbol{\theta}$ is represented by three angles, $\theta,\ \phi,\ \psi$ along the three body axes.

$$\mathbf{x}_{\widehat{INS}} = [\delta Lat,\ \delta lon,\ \delta h,\ \delta v_N,\ \delta v_E,\ \delta v_D,\ \epsilon_x,\ \epsilon_y,\ \epsilon_z]^T \tag{3.16a}$$

$$\mathbf{x}_{\widehat{INS}} = [\delta\mathbf{p},\ \delta\mathbf{v},\ \boldsymbol{\epsilon}]^T \tag{3.16b}$$

where, $\boldsymbol{\epsilon}$, describes tilt errors about the three axes, and $\mathbf{C}_{\tilde{n}}^{n}$ is the direction cosine matrix (DCM) estimated from $\boldsymbol{\epsilon}$, which correct the attitude provided by the IMU. Tracking the error provides better filter stability, because the errors change slowly when compared to the actual system dynamics. Therefore, to obtain an estimate of position, velocity and attitude the EKF vector in Equation (3.16a) needs to be added to the data provided by the IMU. Combining the filter state error estimates $\mathbf{x}_{\widehat{INS}}$ and the data provided by the IMU $\mathbf{x}_{INS}$, an estimate on the true position, velocity and attitude, $\mathbf{x}_{true}$ is obtained.

$$\mathbf{x}_{INS_{true}} = \begin{bmatrix} \mathbf{p}_{true} \\ \mathbf{v}_{true} \\ \boldsymbol{\theta}_{true}^{n} \end{bmatrix} = \begin{bmatrix} \mathbf{p}_{INS} + \delta\mathbf{p} \\ \mathbf{v}_{INS} + \delta\mathbf{v} \\ \mathbf{C}_{\tilde{n}}^{n}(\boldsymbol{\epsilon})\boldsymbol{\theta}_{INS}^{\tilde{n}} \end{bmatrix} \tag{3.17}$$

To determine the position on Earth using inertial measurement data, it is necessary to make some assumptions regarding the shape of the Earth [24]. The Earth is assumed to be an ellipsoid with meridian radius of curvature R_N, given by Equation (3.18), with rotation rate Ω and transverse radius of curvature $C_{\oplus}$, given by Equation (3.19), at latitude L.

$$R_N = R_{\oplus}\frac{1-e^2}{(1-e^2\sin^2 L)^{3/2}} \tag{3.18}$$

$$C_{\oplus} = R_E = \frac{R_{\oplus}}{\sqrt{1-e^2\sin^2 L}} \tag{3.19}$$

where $R_{\oplus}$ is the Earth radius and e is the eccentricity of the Earth.

With the state vector and assumptions regarding the shape of the Earth, Pinson's error model can be used to obtain the dynamics equations describing the INS. The Pinson error model detailed in [24] was rearranged to match the INS state vector $\mathbf{x}_{INS}$ showed in Equation (3.15a), which resulted in Equation (3.20).

$$\mathbf{F}_{INS} = \begin{pmatrix} \mathbf{F}_{pp} & \mathbf{F}_{pv} & \mathbf{F}_{p\epsilon} \\ \mathbf{F}_{vp} & \mathbf{F}_{vv} & \mathbf{F}_{v\epsilon} \\ \mathbf{F}_{\epsilon p} & \mathbf{F}_{\epsilon v} & \mathbf{F}_{\epsilon\epsilon} \end{pmatrix} \tag{3.20}$$

where the subscripts of the matrix $\mathbf{F}_{p,v,\epsilon}$ denote the position, velocity and tilt error, respectively. The matrices of $\mathbf{F}_{INS}$ describing the position error dynamics are defined as

$$\mathbf{F}_{pp} = \begin{pmatrix} 0 & 0 & -\dfrac{v_N}{C_\oplus^2} \\ \dfrac{v_E \tan L}{C_\oplus \cos L} & 0 & -\dfrac{v_E}{C_\oplus^2 \cos L} \\ 0 & 0 & 0 \end{pmatrix} \tag{3.21}$$

$$\mathbf{F}_{pv} = \begin{pmatrix} \dfrac{1}{C_\oplus} & 0 & 0 \\ 0 & \dfrac{1}{C_\oplus \cos L} & 0 \\ 0 & 0 & -1 \end{pmatrix} \tag{3.22}$$

$$\mathbf{F}_{p\epsilon} = \mathbf{0}_{3\times 3} \tag{3.23}$$

The velocity error dynamics equations are defined as

$$\mathbf{F}_{vp} = \begin{pmatrix} -v_E \left(2\Omega \cos L + \dfrac{v_E}{C_\oplus \cos^2 L}\right) & 0 & \dfrac{1}{C_\oplus^2}(v_E^2 \tan L - v_N v_D) \\ 2\Omega(v_N \cos L - v_D \sin L) + \dfrac{v_N v_E}{C_\oplus \cos^2 L} & 0 & -\dfrac{v_E}{C_\oplus^2}(v_N \tan L + v_D) \\ 2\Omega v_E \sin L & 0 & \dfrac{1}{C_\oplus^2}(v_N^2 + v_E^2) \end{pmatrix} \tag{3.24}$$

$$\mathbf{F}_{vv} = \begin{pmatrix} \frac{v_D}{C_\oplus} & -2(\Omega \sin L + \frac{v_E}{C_\oplus} \tan L) & \frac{v_N}{C_\oplus} \\ 2\Omega \sin L + \frac{v_E}{C_\oplus} \tan L & \frac{1}{C_\oplus}(v_N \tan L + v_D) & 2\Omega \cos L + \frac{v_E}{C_\oplus} \\ -\frac{2v_N}{C_\oplus} & -2(\Omega \cos L + \frac{v_E}{C_\oplus}) & 0 \end{pmatrix} \tag{3.25}$$

$$\mathbf{F}_{v\epsilon} = \begin{pmatrix} 0 & -f_D & f_E \\ f_D & 0 & -f_N \\ -f_E & f_N & 0 \end{pmatrix} \tag{3.26}$$

where, $\mathbf{f}_{NED}$ are the specific acceleration forces in the navigation frame. To calculate these forces the rate of change of the latitude, $\dot{L}$, and longitude, $\dot{l}$, defined by Equations (3.27) and (3.28) are needed. These rates are calculated using the known velocity $\mathbf{v}$, expressed in the navigation frame.

$$\dot{L} = \frac{v_N}{R_N + h(t)} \tag{3.27}$$

$$\dot{l} = \frac{v_E \sec L(t)}{C_\oplus + h(t)} \tag{3.28}$$

To subsequently calculate the acceleration, the change in position, Δx is calculated as

$$\Delta\mathbf{x} = \begin{bmatrix} (L(t+\Delta t) - L(t))(R_N + h(t)) \\ (l(t+\Delta t) - l(t))(R_E + h(t))\cos(L(t)) \\ -(h(t+\Delta t) - h(t) \end{bmatrix} \tag{3.29}$$

where Δt is the time interval. From the change in position and the velocity, the acceleration, $\mathbf{a}$, and the forces $\mathbf{f}_{NED}$ that cause that acceleration are calculated as

$$\mathbf{a} = \dot{\mathbf{v}} = 2\frac{\Delta\mathbf{x} - \mathbf{v}\Delta t}{\Delta t^2} \tag{3.30}$$

$$\mathbf{f}_{NED} = \begin{bmatrix} \mathbf{a}_N + v_E(2\Omega + \dot{l}) + \sin(L) - v_D\dot{L} \\ \mathbf{a}_E - v_N(2\Omega + \dot{l})\sin(L) - v_D(2\Omega + \dot{l})\cos(L) \\ \mathbf{a}_z + v_y(2\Omega + \dot{l})\cos(L) - v_N\dot{L} - g \end{bmatrix} \tag{3.31}$$

The equations describing the tilt error dynamics as a function of the states is defined as

$$\mathbf{F}_{\epsilon p} = \begin{pmatrix} -\Omega\sin L & 0 & -\dfrac{v_E}{C_\oplus^2} \\ 0 & 0 & \dfrac{v_N}{C_\oplus^2} \\ -\Omega\cos L - \dfrac{v_E}{C_\oplus\cos^2 L} & 0 & \dfrac{v_E\tan L}{C_\oplus^2} \end{pmatrix} \tag{3.32}$$

$$\mathbf{F}_{\epsilon v} = \begin{pmatrix} 0 & \dfrac{1}{C_\oplus} & 0 \\ -\dfrac{1}{C_\oplus} & 0 & 0 \\ 0 & -\dfrac{\tan L}{C_\oplus} & 0 \end{pmatrix} \tag{3.33}$$

$$\mathbf{F}_{\epsilon\epsilon} = \begin{pmatrix} 0 & -\Omega\sin L - \dfrac{v_E}{C_\oplus}\tan L & \dfrac{v_N}{C_\oplus} \\ \Omega\sin L + \dfrac{v_E}{C_\oplus}\tan L & 0 & \Omega\cos L + \dfrac{v_E}{C_\oplus} \\ -\dfrac{v_N}{C_\oplus} & -\Omega\cos L - \dfrac{v_E}{C_\oplus} & 0 \end{pmatrix} \tag{3.34}$$

To completely model the errors generated by the IMU, the three accelerometer biases, $\mathbf{b}_a$, three gyroscope biases, $\mathbf{b}_g$, are modeled as showed in Equations (3.8) and (3.13), respectively.

Augmenting the state vector from Equation (3.16a) with these biases yields the new augmented state vector as

$$\mathbf{x}_{IMU} = [\delta\mathbf{p}, \delta\mathbf{v}, \mathbf{C}_{\tilde{n}}^{n}(\boldsymbol{\epsilon}), \mathbf{b}_a, \mathbf{b}_g]^T \tag{3.35}$$

Using the model shown in Equations (3.8) and (3.13), the continuous-time dynamics matrices describing it are defined as

$$\mathbf{F}_{b_a} = \mathbf{I}_{3\times3} \cdot -\frac{1}{\tau_a} \tag{3.36}$$

$$\mathbf{F}_{b_g} = \mathbf{I}_{3\times3} \cdot -\frac{1}{\tau_g} \tag{3.37}$$

Combining these new continuous-time dynamics Equations (3.36), (3.37) and (3.47) with $\mathbf{F}_{INS}$ from Equation (3.20), results in $\mathbf{F}_{IMU}$, which describes the continuous-time dynamics of the error propagation for the IMU.

$$\mathbf{F}_{IMU} = \begin{pmatrix} \mathbf{F}_{INS} & \mathbf{0}_{9\times3} & \mathbf{0}_{9\times3} \\ \mathbf{0}_{3\times9} & \mathbf{F}_{b_a} & \mathbf{0}_{3\times3} \\ \mathbf{0}_{3\times9} & \mathbf{0}_{3\times3} & \mathbf{F}_{b_g} \end{pmatrix} \tag{3.38}$$

With the continuous-time dynamic matrix defined, it is necessary to combine the continuous-time noise equations into a matrix to form $\mathbf{Q}_{IMU}$. Which is obtained by combining Equations (3.6), (3.9), (3.11) and (3.14).

$$\mathbf{Q}_{IMU} = \begin{pmatrix} \mathbf{0}_{3\times3} & \mathbf{0}_{3\times3} & \mathbf{0}_{3\times3} & \mathbf{0}_{3\times3} & \mathbf{0}_{3\times3} \\ \mathbf{0}_{3\times3} & \mathbf{C}_n^b q_a \mathbf{I}_{3\times3} {\mathbf{C}_n^b}^T & \mathbf{0}_{3\times3} & \mathbf{0}_{3\times3} & \mathbf{0}_{3\times3} \\ \mathbf{0}_{3\times3} & \mathbf{0}_{3\times3} & \mathbf{C}_n^b q_g \mathbf{I}_{3\times3} {\mathbf{C}_n^b}^T & \mathbf{0}_{3\times3} & \mathbf{0}_{3\times3} \\ \mathbf{0}_{3\times3} & \mathbf{0}_{3\times3} & \mathbf{0}_{3\times3} & \frac{2\sigma_{b_a}^2}{\tau_a}\mathbf{I}_{3\times3} & \mathbf{0}_{3\times3} \\ \mathbf{0}_{3\times3} & \mathbf{0}_{3\times3} & \mathbf{0}_{3\times3} & \mathbf{0}_{3\times3} & \frac{2\sigma_{b_g}^2}{\tau_g}\mathbf{I}_{3\times3} \end{pmatrix} \tag{3.39}$$

with its distribution matrix, $\mathbf{G}_{IMU}$.

$$\mathbf{G}_{IMU} = \mathbf{I}_{15\times15} \tag{3.40}$$

3.5.2 Barometric Altimeter Model

The barometric altimeter measures the altitude of the sensor. This system can be modeled as the sum of the true altitude, a FOGM bias and AWGN.

$$h_{baro}(t) = h_{true}(t) + b_b(t) + w_b(t) \tag{3.41}$$

where the AWGN is defined by

$$E[w_b(t)] = 0 \tag{3.42}$$

$$E[w_b(t)w_b(t+\tau)] = \sigma_b^2\delta(\tau) \tag{3.43}$$

and the FOGM process defined by

$$\dot{b}_b(t) = -\frac{1}{\tau_b}b_b(t) + w_{b_b} \tag{3.44}$$

$$E[w_{b_b}(t)] = 0 \tag{3.45}$$

$$E[w_{b_b}(t)w_{b_b}(t+\tau)] = \frac{2\sigma_{b_b}^2}{\tau_b}\delta(\tau) \tag{3.46}$$

From Equation (3.44) we defined $\mathbf{F}_{b_b}$, and from Equation (3.46), $\mathbf{Q}_{b_b}$, as

$$F_{b_b} = -\frac{1}{\tau_b} \tag{3.47}$$

$$Q_{b_b} = \sigma_b^2 \tag{3.48}$$

3.5.3 Star Tracker Model

Star tracker provides topocentric RA and DEC angles, $\mathbf{\Lambda}$. The star tracker is modeled as the sum of the true angles, a FOGM bias and zero-mean AWGN. The bias, $\mathbf{b}_s$, represents the bias due to the RSO ephemeris error which the reference site is measuring. The noise, $\mathbf{w}_s$, is the noise introduced by the sensor, which it was assumed both sites (reference and remote) use same quality sensor with same noise strength.

$$\mathbf{\Lambda} = \mathbf{\Lambda}_{true} + \mathbf{b}_s + \mathbf{w}_s \tag{3.49}$$

where the AWGN is defined by

$$E[\mathbf{w}_s(t)] = 0 \tag{3.50a}$$

$$E[\mathbf{w}_s(t)\mathbf{w}_s(t+\tau)] = q_s\mathbf{I}_{2\times 2}\delta(\tau) \tag{3.50b}$$

$$E[\mathbf{w}_s(t)\mathbf{b}_s(t+\tau)] = \mathbf{0}_{2\times 2} \tag{3.51}$$

and the bias FOGM process defined by

$$\dot{\mathbf{b}}_s(t) = -\frac{1}{\tau_s}\mathbf{b}_s(t) + \mathbf{w}_{b_s} \tag{3.52}$$

$$E[\mathbf{w}_{b_s}(t)] = 0 \tag{3.53a}$$

$$E[\mathbf{w}_{b_s}(t)\mathbf{w}_{b_s}(t+\tau)] = \frac{2\sigma_{b_s}^2}{\tau_s}\mathbf{I}_{2\times 2}\delta(\tau) \tag{3.53b}$$

With the star tracker bias model presented in Equation (3.52) we defined, $\mathbf{F}_{b_s}$, and with the noise strength shown in Equation (3.53b), we defined $\mathbf{Q}_{b_s}$, as

$$\mathbf{F}_{b_s} = \begin{pmatrix} -\frac{1}{\tau_s} & 0 \\ 0 & -\frac{1}{\tau_s} \end{pmatrix} \tag{3.54}$$

$$\mathbf{Q}_{b_s} = \begin{pmatrix} \frac{2\sigma_{b_s}^2}{\tau_s} & 0 \\ 0 & \frac{2\sigma_{b_s}^2}{\tau_s} \end{pmatrix} \tag{3.55}$$

3.5.4 Complete System Dynamics Model

Combining the dynamics models presented in Sections 3.5.1 to 3.5.3, we combine the state vectors presented in those sections to define the system state vector, $\mathbf{x}$, as

$$\mathbf{x} = [\delta Lat,\ \delta lon,\ \delta h,\ \delta v_N,\ \delta v_E,\ \delta v_D,\ \epsilon_x,\ \epsilon_y,\ \epsilon_z, b_{a_x}, b_{a_y}, b_{a_z}, b_{g_x}, b_{g_y}, b_{g_z}, b_\alpha, b_\delta, b_b]^T \tag{3.56a}$$

$$\mathbf{x} = [\delta\mathbf{p}, \delta\mathbf{v}, \boldsymbol{\epsilon}, \mathbf{b}_a, \mathbf{b}_g, \mathbf{b}_s, b_b]^T \tag{3.56b}$$

where $\delta\mathbf{p}$ is the error in position given by geodetic latitude, longitude and altitude. Velocity error in the local level NED frame, relative to the Earth is described by $\delta\mathbf{v}$. The tilt errors about the three axis are described by, $\boldsymbol{\epsilon}$ and $\mathbf{C}_{\tilde{n}}^{n}$ is the DCM estimated from $\boldsymbol{\epsilon}$, which correct the attitude provided by the IMU. The biases for the accelerometers, gyroscopes, star tracker and altimeter are represented by, $\mathbf{b}_a$, $\mathbf{b}_g$, $\mathbf{b}_s$, and b_b, respectively. With the state vector for the entire system defined, the $\mathbf{F}$ matrix that describes the continuous-time dynamics and the continuous-time noise strength matrix, $\mathbf{Q}$, are described by

$$\mathbf{F} = \begin{pmatrix} \mathbf{F}_{INS} & \mathbf{0}_{9\times3} & \mathbf{0}_{9\times3} & \mathbf{0}_{9\times2} & \mathbf{0}_{9\times1} \\ \mathbf{0}_{3\times9} & \mathbf{F}_{b_a} & \mathbf{0}_{3\times3} & \mathbf{0}_{3\times2} & \mathbf{0}_{3\times1} \\ \mathbf{0}_{3\times9} & \mathbf{0}_{3\times3} & \mathbf{F}_{b_g} & \mathbf{0}_{3\times2} & \mathbf{0}_{3\times1} \\ \mathbf{0}_{2\times9} & \mathbf{0}_{2\times3} & \mathbf{0}_{2\times3} & \mathbf{F}_{b_s} & \mathbf{0}_{2\times1} \\ \mathbf{0}_{1\times9} & \mathbf{0}_{1\times3} & \mathbf{0}_{1\times3} & \mathbf{0}_{1\times2} & F_{b_b} \end{pmatrix} \tag{3.57}$$

$$\mathbf{Q} = \begin{pmatrix} \mathbf{0}_{3\times3} & \mathbf{0}_{3\times3} & \mathbf{0}_{3\times3} & \mathbf{0}_{3\times3} & \mathbf{0}_{3\times3} & \mathbf{0}_{3\times2} & \mathbf{0}_{3\times1} \\ \mathbf{0}_{3\times3} & \mathbf{C}_n^b q_a \mathbf{I}_{3\times3} {\mathbf{C}_n^b}^T & \mathbf{0}_{3\times3} & \mathbf{0}_{3\times3} & \mathbf{0}_{3\times3} & \mathbf{0}_{3\times2} & \mathbf{0}_{3\times1} \\ \mathbf{0}_{3\times3} & \mathbf{0}_{3\times3} & \mathbf{C}_n^b q_g \mathbf{I}_{3\times3} {\mathbf{C}_n^b}^T & \mathbf{0}_{3\times3} & \mathbf{0}_{3\times3} & \mathbf{0}_{3\times2} & \mathbf{0}_{3\times1} \\ \mathbf{0}_{3\times3} & \mathbf{0}_{3\times3} & \mathbf{0}_{3\times3} & \frac{2\sigma_{b_a}^2}{\tau_a}\mathbf{I}_{3\times3} & \mathbf{0}_{3\times3} & \mathbf{0}_{3\times2} & \mathbf{0}_{3\times1} \\ \mathbf{0}_{3\times3} & \mathbf{0}_{3\times3} & \mathbf{0}_{3\times3} & \mathbf{0}_{3\times3} & \frac{2\sigma_{b_g}^2}{\tau_g}\mathbf{I}_{3\times3} & \mathbf{0}_{3\times2} & \mathbf{0}_{3\times1} \\ \mathbf{0}_{2\times3} & \mathbf{0}_{2\times3} & \mathbf{0}_{2\times3} & \mathbf{0}_{2\times3} & \mathbf{0}_{2\times3} & \frac{2\sigma_{b_s}^2}{\tau_s}\mathbf{I}_{2\times2} & \mathbf{0}_{2\times1} \\ \mathbf{0}_{1\times3} & \mathbf{0}_{1\times3} & \mathbf{0}_{1\times3} & \mathbf{0}_{1\times3} & \mathbf{0}_{1\times3} & \mathbf{0}_{3\times2} & \frac{2\sigma_{b_b}^2}{\tau_b} \end{pmatrix} \tag{3.58}$$

with its distribution matrix, **G**.

$$\mathbf{G} = \mathbf{I}_{18\times18} \tag{3.59}$$

Using Equation (2.21) to calculate $\mathbf{\Phi}$ and $\mathbf{Q}$ can be discretized using Equation (2.24), generating $\mathbf{Q}_d$. With $\mathbf{Q}_d$, the covariance of the system can be propagated forward in time by the EKF. The parameters used in our work for the IMU and star tracker needed to simulate data, are listed in Table 1. These parameters typical for tactical grade IMU and currently available COTS star trackers. The equations presented in this section described the dynamics of the system, in the following section the measurement model used for the EKF is presented.

3.5.5 Measurement Model

The three measurements incorporated by the EKF are altitude from barometric altimeter, angles measured from observer to imaged satellite, and angle correction from the reference site. The angle measurements from the observer to the imaged satellite are independent from the reference site corrections. The measurement model for the barometric altimeter was defined from Equation (3.41) and using the model

Table 1. **Sensors parameters.**

Name	Symbol	Value	Units
Accelerometer Bias	σ_{b_a}	9.8×10^{-3}	m/s^2
Gyroscope Bias	σ_{b_g}	4.84×10^{-6}	rad/s
Gyro/Accel Time Correlation	$\tau_{a,g}$	3600	s
Barometric Altimeter Bias	σ_b	5	m
Star Tracker Accuracy	$\sigma_{b_s,st1}$	4.84×10^{-6}	rad
Star Tracker Time Correlation	τ_s	120	s

presented in Equation (2.16).

$$z_{baro}(t_i) = \mathbf{H}_{baro}(t_i)\mathbf{x}(t_i) + b_b + \mathrm{v}_b(t_i) \tag{3.60}$$

The measurement model for the barometric altimeter is linear. Therefore, the mapping to the corresponding state $\mathbf{H}_{baro}$ was done directly without linearizing.

$$\mathbf{H}_{baro} = \begin{bmatrix} 0 & 0 & 1 & \mathbf{0}_{1\times 14} & 1 \end{bmatrix} \tag{3.61}$$

with its measurement uncertainty R_{baro} given by

$$R_{baro}(t_i) = E[\mathrm{v}_b(t_i)\mathrm{v}_b(t_j)] = \sigma_{bm}^2 \tag{3.62}$$

The star tracker will be modeled with two distinct models. The first model $\mathbf{z}_{st1}$, describes the measured topocentric right ascension and declination, as

$$\mathbf{z}_{st1}(t_i) = \mathbf{h}_{st1}(t_i)[\widehat{\mathbf{x}}(t_i), t_i] + \mathbf{b}_{st} + \mathbf{v}_{st1}(t_i) \tag{3.63}$$

$$\mathbf{R}_{st1}(t_i) = E[\mathbf{v}_{st1}(t_i)\mathbf{v}_{st1}^T(t_i)] = \begin{pmatrix} \sigma_{st1}^2 & 0 \\ 0 & \sigma_{st1}^2 \end{pmatrix} \tag{3.64}$$

where the variance $\sigma_{st1} = \sigma_{b_s}$, as listed in Table 1, which is the accuracy of the star tracker. The measurement model $\mathbf{h}_{st1}$, is described by the non-linear Equation (3.65). The measurement equations are a function of ρ, which is the magnitude of the pointing vector $\mathbf{P}$ from the observer to the RSO in the ECEF frame, as explained in Section 3.2 [25].

$$\mathbf{h}_{st1}(t_i) = \begin{bmatrix} \alpha \\ \delta \end{bmatrix} = \begin{bmatrix} \tan^{-1}\left(\dfrac{P_y}{P_x}\right) \\ \sin^{-1}\left(\dfrac{P_z}{\rho}\right) \end{bmatrix} \tag{3.65}$$

The angles are non-linear functions of the state. In order to implement this model in the EKF algorithm, the equations must be linearized around the current state as showed in Equation (2.26). Linearizing $\mathbf{h}_{st1}$ around the current state, yields $\mathbf{H}_{st1}$ shown below

$$\mathbf{H}_{st1}(t_{i+1}) \triangleq \left.\frac{\partial \mathbf{h}_{st1}(\delta\mathbf{x}, t)}{\partial \delta\mathbf{x}(t)}\right|_{\delta\mathbf{x}=\widehat{\mathbf{x}}(t_{i+1}^-)} \tag{3.66a}$$

$$= \begin{pmatrix} \dfrac{\partial\alpha}{\partial\delta L} & \dfrac{\partial\alpha}{\partial\delta l} & \dfrac{\partial\alpha}{\partial\delta h} & \mathbf{0}_{1\times12} & 1 & 0 & 0 \\ \dfrac{\partial\delta}{\partial\delta L} & \dfrac{\partial\delta}{\partial\delta l} & \dfrac{\partial\delta}{\partial\delta h} & \mathbf{0}_{1\times12} & 0 & 1 & 0 \end{pmatrix} \tag{3.66b}$$

the complete derivation of $\mathbf{H}_{st1}$ are found in Appendix A. The linearization $\mathbf{H}_{st1}$ derived in the appendix and presented here differs from the one presented by Pierce [19]. The difference between the two is how $\mathbf{h}_{st1}$ was defined, particularly the trigonometric equation used for the right ascension. As depicted in Equation (3.65), the right ascension equation used in this thesis involves arctan, where Pierce used arcsin $\left(\frac{P_y}{\sqrt{P_x^2+P_y^2}}\right)$ [19]. Both equations are equivalent to calculate the right ascension and can be found in [25]. However, when linearizing this non-linear equations information about the quadrant is lost. Since RA is defined from $0-2\pi$, quadrant information is critical. For this reason arctan was used in this thesis in lieu of arcsin. To retain the quadrant information when linearizing $\mathbf{h}_{st1}$, arctan was treated as a function of two variables, in this case P_y and P_x. Treating the trigonometric function as a function of two variables result in two partial derivatives, retaining information about the quadrant. This approach of treating arctan as a function of two variable is equivalent of using atan2 in computer language. Therefore, when implementing this measurement model in MATLAB®the atan2 function was used. To emphasize this difference atan2 was used in the notation at the beginning of this chapter and in the appendix.

The second measurement model for the star tracker $\mathbf{z}_{st2}$, describes the angle correction received from the reference site, which is a direct measurement of the bias, $\mathbf{b}_s$ in addition to AWGN, $\mathbf{v}_{st2}$.

$$\mathbf{z}_{st2}(t_i) = \mathbf{h}_{st2}(t_i)[\widehat{\mathbf{x}}(t_i), t_i] + \mathbf{v}_{st2}(t_i) \tag{3.67}$$

$$\mathbf{R}_{st2}(t_i) = E[\mathbf{v}_{st2}(t_i)\mathbf{v}_{st2}^T(t_i)] = \begin{pmatrix} \sigma_{st2}^2 & 0 \\ 0 & \sigma_{st2}^2 \end{pmatrix} \tag{3.68}$$

σ_{st2} is dependent on the reference site sensor noise since the bias is measured at the reference site. The transformation matrix $\mathbf{W}$ is used on the white Gaussian noise from the sensor at the reference site $\mathbf{V}_d$ and taking the expected value, yields

Equation (3.69)which is the reference site's variance projected to the remote site.

$$E[(\mathbf{W}\mathbf{v}_d)(\mathbf{W}\mathbf{v}_d)^T] = \mathbf{W}E[\mathbf{v}_d\mathbf{v}_d^T]\mathbf{W}^T \tag{3.69}$$

It was assumed the reference site and the remote site use same quality sensor. Therefore, the variance for the reference site is also given by σ_{st1} and when projected to the remote is given by σ_{st2} defined by Equation (3.70).

$$\sigma_{st2}^2 = \mathbf{W}\sigma_{st1}^2\mathbf{I}\mathbf{W}^T \tag{3.70}$$

As stated before, $\boldsymbol{\Delta\theta}_{remote}$ is directly related to $\mathbf{b}_s$, which this bias represents the ephemeris error. This measurement consists of the $\boldsymbol{\Delta\theta}_{reference}$ projected to the remote site using $\mathbf{W}$ showed in Equation (2.14). This bias is included in the state vector $\mathbf{x}$, for this reason $\mathbf{H}_{st2}$ becomes a direct mapping to those states, as shown in Equation (3.72b).

$$\mathbf{h}_{st2}(t_i) = \begin{bmatrix} \Delta\alpha_{remote} \\ \Delta\delta_{remote} \end{bmatrix} = \begin{bmatrix} b_{s_\alpha} \\ b_{s_\delta} \end{bmatrix} \tag{3.71}$$

$$\mathbf{H}_{st2}(i+1) \triangleq \left.\frac{\partial \mathbf{h}_{st2}(\delta\mathbf{x}, t)}{\partial \delta\mathbf{x}(t)}\right|_{\delta\mathbf{x}=\widehat{\mathbf{x}}(t_{i+1}^-)} \tag{3.72a}$$

$$= \begin{pmatrix} \mathbf{0}_{1\times 15} & 1 & 0 & 0 \\ \mathbf{0}_{1\times 15} & 0 & 1 & 0 \end{pmatrix} \tag{3.72b}$$

3.6 SPIDER

The Kalman filter algorithm was implemented using Sensor Processing for Inertial Dynamics Error Reduction (SPIDER). SPIDER is a navigation based Kalman filtering software developed by the Autonomy & Navigation Technology (ANT) center at the Air Force Institute of Technology (AFIT)[10]. The benefit of using SPIDER rather than developing an independent algorithm for this thesis is that SPIDER is modular, relatively easy to introduce additional sensors, and most importantly it is a proven tool. Most sensors used in this research are options currently modeled and available for use in SPIDER. The only sensor not currently modeled is the star tracker with its two form of measurement previously described in Section 3.5.3. Following SPIDER interface control document (ICD)[1], the required MATLAB® functions were written to incorporate the star tracker sensor to SPIDER.

3.7 Summary

This chapter developed the model of integrating a star tracker, IMU and baro measurement with an EKF to evaluate the performance improvement of correcting for satellite ephemeris with the presented technique. The next chapter compares and analyzes the results of the navigation states estimates for the different scenarios with different combinations of distance and time delays.

IV. Results

4.1 Introduction

This chapter presents the results obtained from simulations of the model described in Chapter III. First, the results obtained from varying the baseline distance from the reference site and remote site are shown. Secondly, following the same methodology, results depicting the effects of adding time delay to the transformation matrix are compared. The time delay effects are also combined with varying distances between the reference and remote sites. Finally, the results of the navigation states from the EKF are presented in this chapter. The results of the EKF are compared between free INS and incorporating star tracker measurements.

4.2 Distance Variant Results

First, we used the simulated data to validate the transformation matrix $\mathbf{W}$ presented in Equation (2.14). The method compared the remote site's measured angles with the reference site's angles projected to the remote site's image frame using $\mathbf{W}$. To validate $\mathbf{W}$, the transformation matrix must accurately project the angle correction $\delta\boldsymbol{\theta}$ to the remote site. The results obtained from applying the transformation matrix $\mathbf{W}$ are shown in Figure 4. The results validate the methodology proposed by Pierce [19] and presented earlier in Section 2.4. The projected angles are not exactly equal as shown in Figure 5 , this difference was attributed to the AWGN with variance σ_{b_s}, being introduced by the sensor accuracy at the reference site. When the two sites are co-located this residual is expected to be minimum and within the variance of the sensor.

With the transition matrix $\mathbf{W}$ validated for the co-located scenario more investigation was done to analyze the effects of increasing the baseline distance between the

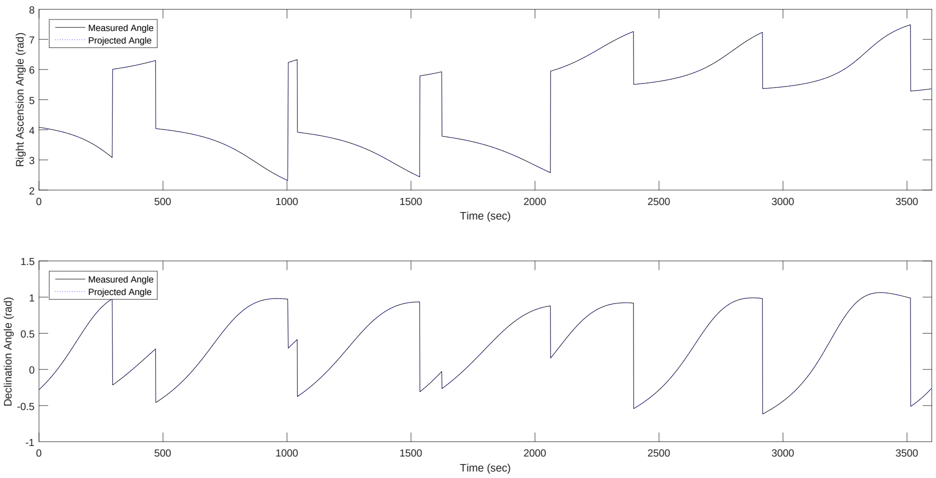

Figure 4. Topocentric right ascension (top) and declination (bottom) angles from 100 km separated sites. Solid lines are simulated angles at remote site, while dotted line is the expected angle at the remote plus the correction from the remote projected.

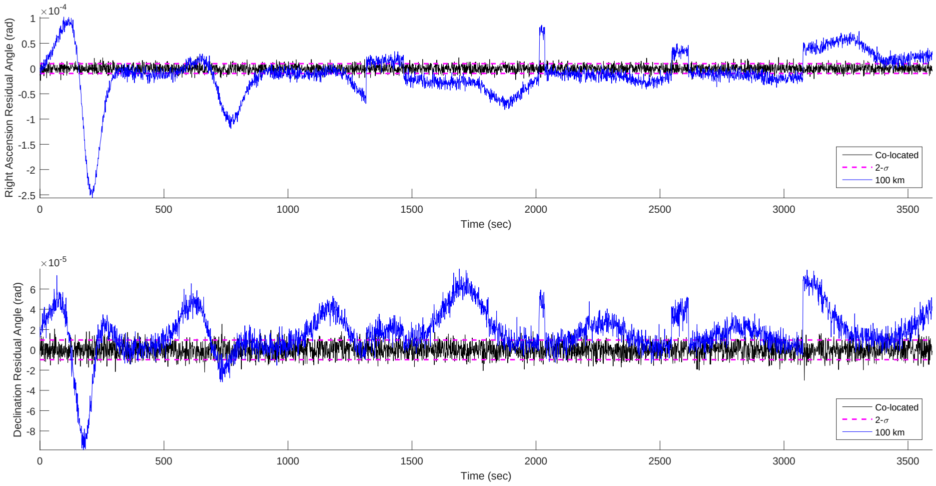

Figure 5. Topocentric right ascension (top) and declination (bottom) angles residuals from co-located site and 100 km separated site. Black lines are the residuals angles from the co-located site, while blue are the residuals from the site separated by 100 km and dotted magenta lines is $2 - \sigma$ from the noise introduced by the sensor. At large separation distances, the projected correction does not correct for all angle error.

reference and remote sites. A variety of scenarios started with the remote co-located with the reference, to a maximum distance of 2000 km. 2000 km is approximately the radius of the access area for a RSO in LEO and a minimum elevation angle of 10°. In addition to the distance increase, the heading angle relative to the reference site was

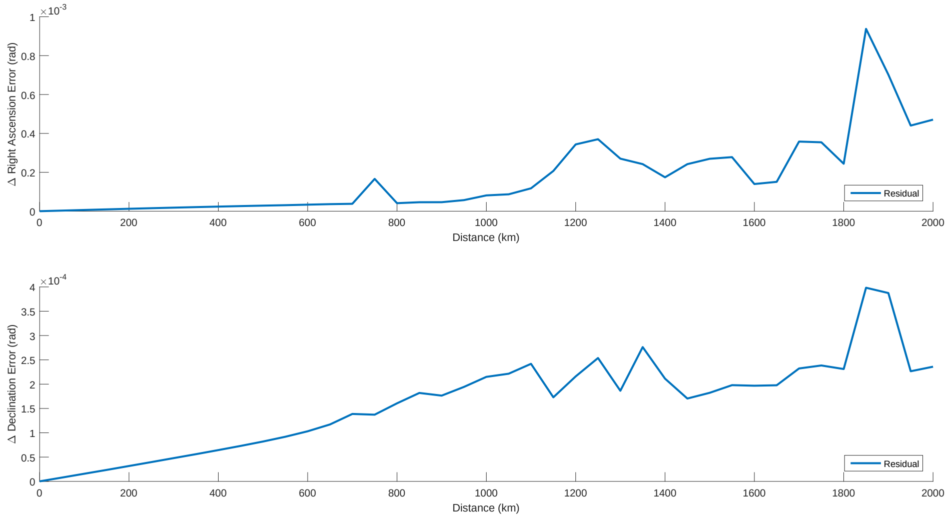

Figure 6. Topocentric right ascension and declination residual angles from sites with increasing baseline distance up to 2000km.

also changed in 45° increments. This heading angle is defined from 0° to 360°, where 0° is North relative to the reference site and continuous clockwise.

The results obtained, showed the transformation **W** properly projects the measured angles from the reference frame to the remote site's image frame when the two sites are co-located, as depicted in Figure 5. The error in the transformed angles increased with larger separation distances between the reference and the remote site, as depicted in Figure 5. This trend of increasing residual error with increased distance continued for the different scenarios simulated. Figure 6 depicts this trend. The data shown is the root mean squared (RMS) of the residual at each distance across all heading angles simulated with no time delays.

These results validated the use of **W** as a method of projecting measured angles with high accuracy with relatively close distances. This decrease in accuracy with longer baseline distances was expected. With larger baseline distances, the geometry changes are more dramatic between the two sites. When this difference in geometry occurs, the information related from one site to the other does not add valuable information. Depending on the application and error tolerance the results shown Figure 6 can be used to determine the threshold distance not to exceed when using this method.

4.3 Time Variant Results

Similar to the effect of distance to the transformation, simulated data was used to analyze the effects of applying the transformation matrix **W** when calculated using observations made at a previous time. RSOs in LEO orbit travel at high velocity, which result in a short window of visibility for an observer on the surface of the Earth. The RSO used in these simulations had an average visibility window of 10 minutes. With this relatively short visibility window, it was expected for time delays to have a greater impact on the transformation when compared to increasing distance, because the pointing angle to the RSO will change significantly in a short period of time. Figure 7 shows how for a particular simulation with the two sites co-located time delays affect the transformation matrix accuracy. During the simulations the transformation matrix was calculated using time delays ranging from 0 to 30 seconds with 10 seconds increments. These results were expected and this trend was expected to continue for larger baseline distances.

Based on the the scenario setup assumed for this research, it is more likely that the reference site is not co-located with the remote. Therefore, the effects of applying an angle correction observed at a previous time, varying from 0 to 30 seconds in the past, in addition to baseline distance were compared. Figure 7 shows a linear growth of the residual for both RA and DEC. It is of interest to show how this error translates when the sites are not co-located. Figure 8 depicts the residual of the transformed angle for distances up to 2000 km and up to 30 s time delays. These results showed that on average an increase of time delay in the calculation of the transformation matrix **W**,

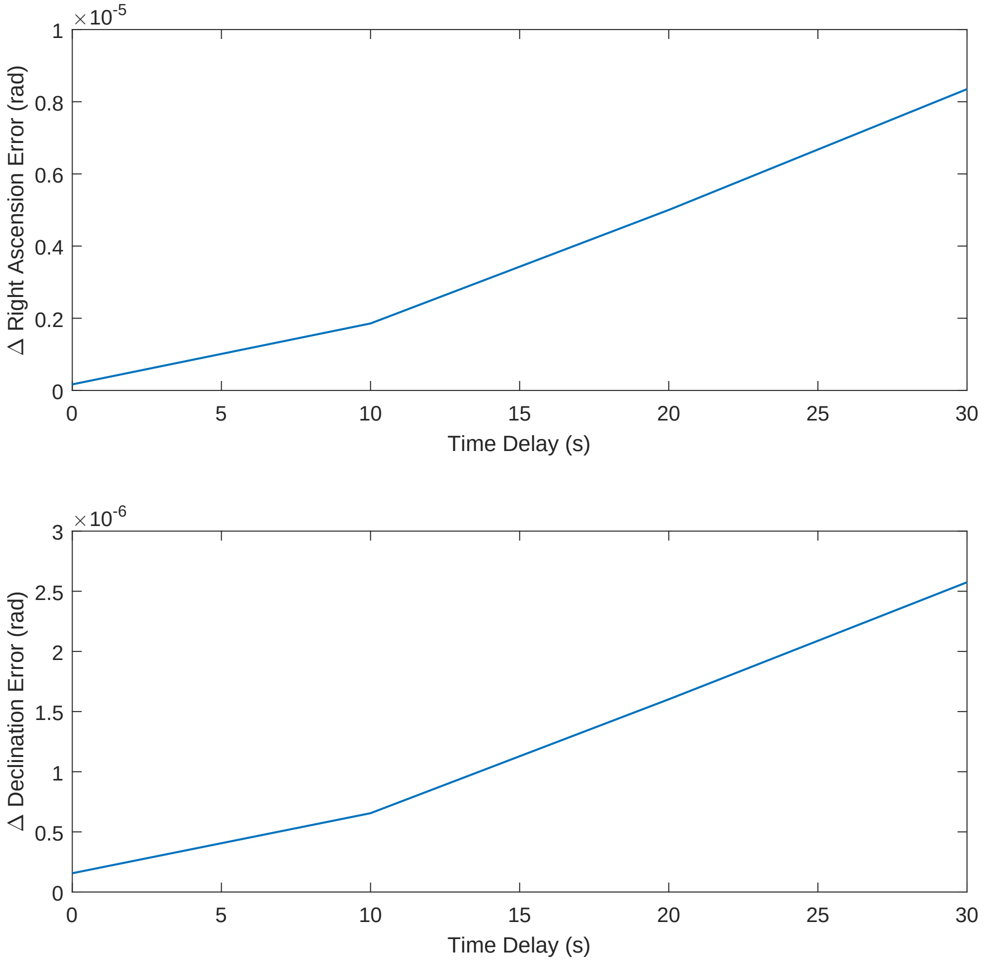

Figure 7. Topocentric right ascension (top) and declination (bottom) residual angles in radians from co-located sites with time delays from 0-30 seconds.

also increases the error in the transformed angles. Figure 8 shows the residual for both RA and DEC linearly growing up to approximately 600 km. For distances greater than 600 km the residual continues to grow in an unpredictable manner. In addition the residual at 600 km is approximately $3.3 \times 10^{-}5$ which results in large positioning error. To put the magnitude in of the residual in perspective, $4.8 \times 10^{-}6$ rad error in the pointing angle for satellites at 1000 km, results in approximately 20 m of error in the observer's position error [19]. For these reasons the area of analysis was limited to distances under 600 km, as depicted in Figure 9.

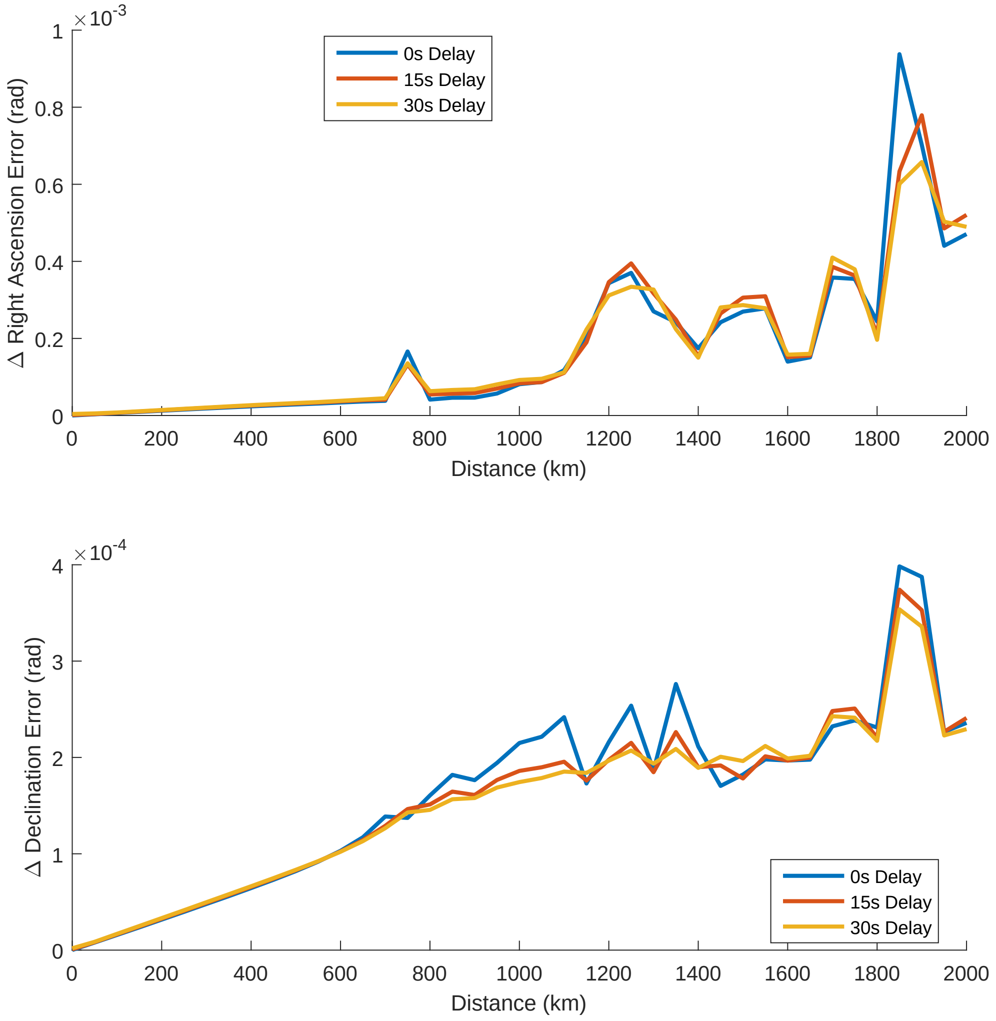

Figure 8. Topocentric right ascension and declination residual angles from sites with increasing baseline distance up to 2000km and time delays from 0s to 30s.

The following section will present and analyze how this increase in error of the transformed angles affects the navigation states calculated by the EKF.

4.4 EKF Results

Sections 4.2 and 4.3 showed the effects of applying the transformation matrix **W** at different distances and time delays. In this section, the results of incorporating

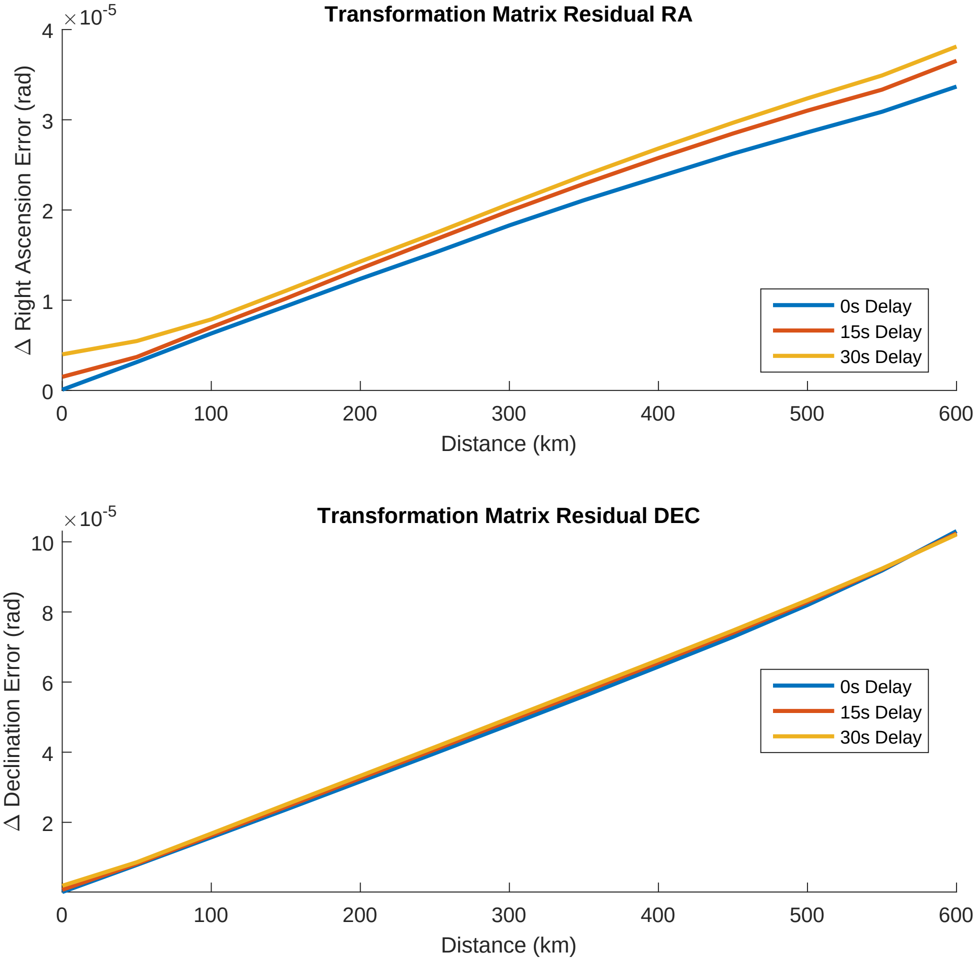

Figure 9. Topocentric right ascension and declination residual angles from sites with baseline distances under 600km and time delays from 0s to 30s.

different measurements into the EKF as well as transformation matrices with time delays are presented. Using the measurement model presented in Section 3.5.5, the performance of the EKF was compared when using free INS, incorporating the star tracker measurements, and finally adding the bias update or ephemeris correction from the reference site.

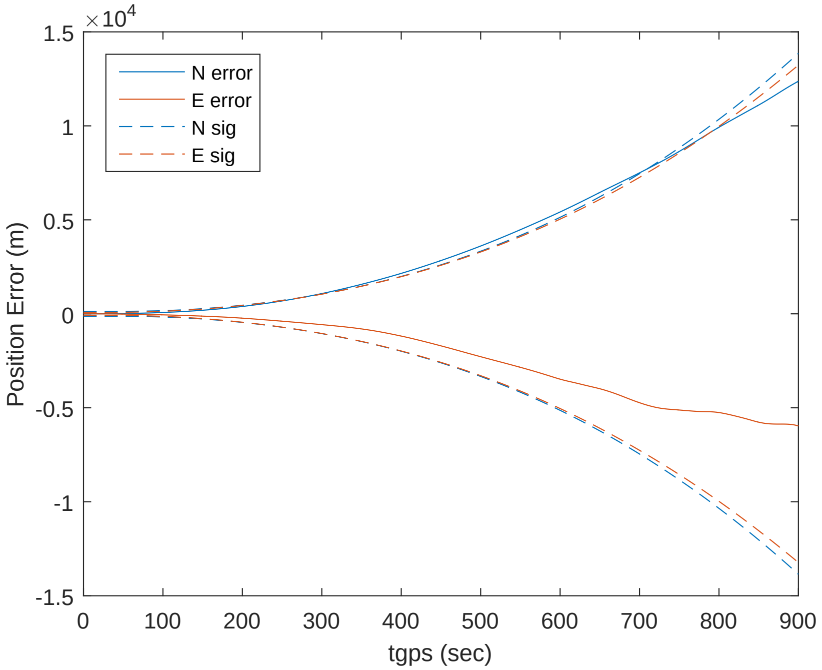

Figure 10. EKF North (blue) and East (red) position estimate errors with only barometric altimeter updates. Dotted lines denote 2-σ variances in each direction.

4.4.1 Free INS

Table 1 shows the parameters used for the EKF simulations. Figure 10 depicts the position error on both North and East axis for the free INS simulation. This simulation run was labeled as free INS, because it is the INS coupled with a barometric altimeter without incorporating any star tracker measurements. A barometric altimeter was included to constrain the vertical drift of the INS, while allowing horizontal drift. The error on the Down axis was omitted in Figure 10 because it was kept relatively constant by the baro within the standard deviation specified in Table 1. With no additional measurements providing updates to the East and North axis, free INS results are consistent with a drifting INS. The simulation was run for 15 min. For this particular simulation the DRMS error was approximately 6333 m. This much error in the navigation states are too large for practical applications. These results are compared in the next section to the same trajectory, but integrating star tracker angle only measurements without the bias updates.

4.4.2 Angles Only

The position estimate was further evaluated when including measurements from the star tracker. The measurements follow the model presented in Section 3.5.5, $\mathbf{z}_{st1}$, which measures the topocentric right ascension and declination from the observer to a RSO of interest. As presented and derived in that section, these measurements provide an update on the position states. Therefore, when incorporating these measurements an improvement in the position estimation was expected. Since there is still a bias in the measurement model due to satellite position error, which is not being updated by this measurement update, error in the form of FOGM process is still expected to be present in the results in addition to the sensor noise. Figure 11 shown below depicts the position error of the navigation states estimated by the EKF incorporating the star tracker pointing angles at 1 Hz.

The DRMS error for this particular simulation run is approximately 2670 m. When these results are compared to the results shown in Figure 10, the position error is reduced by 58%. Even with this significant reduction in the position error, it is still high for navigation applications. It is important to note after approximately 300 seconds the East and North error are outside the 2-σ bound, which indicates the EKF is overconfident. After 700 seconds it appears as the error is reducing to be within the variance bounds, but with such large covariance is not practical for navigation purposes.

4.4.3 Angles and Ephemeris Updates

Using the same trajectory as the one for the previous scenarios, the model was further refined to include measurements from the reference site containing updates for

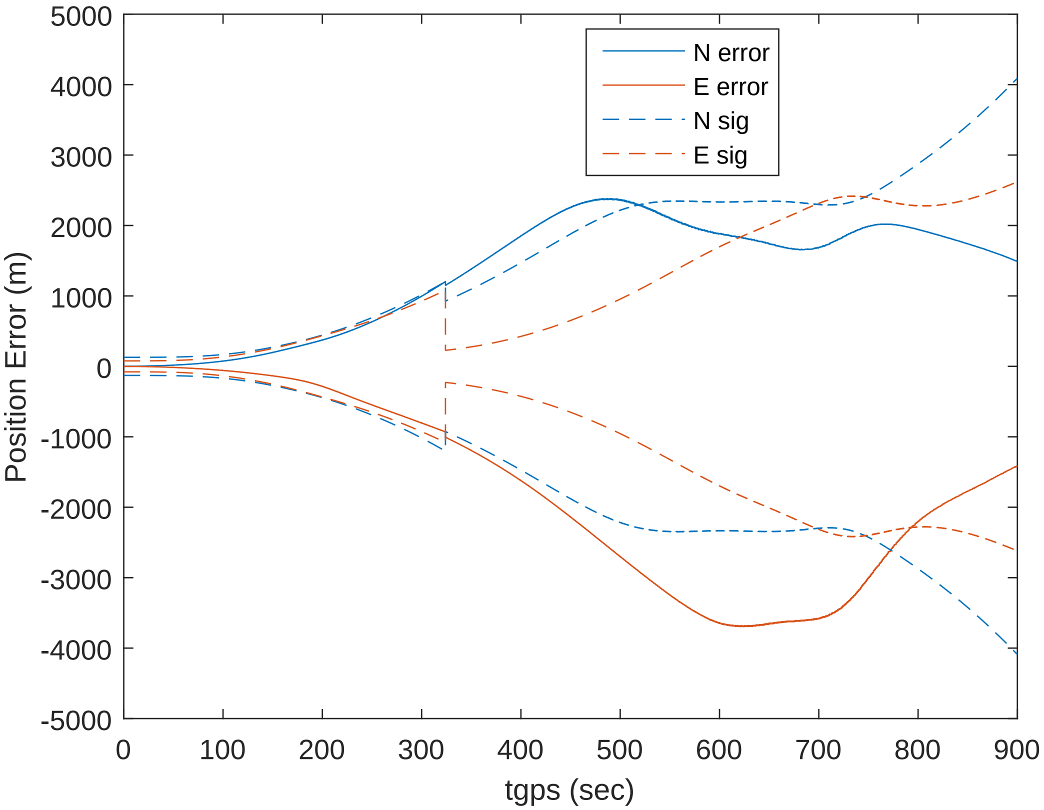

Figure 11. EKF North (blue) and East (red) position estimate errors with baro and 1 Hz star tracker angle updates without ephemeris updates. Dotted lines denote 2-σ variances in each direction.

the bias in the measurement model. Figure 12 depicts the position error in the North and East axis as estimated by the EKF. The parameters used in the filter are the same as for the previous simulations, which are listed in Table 1. For this simulation, the EKF incorporates angles only updates at 1 Hz as in the previous simulation, and the ephemeris correction or bias update is measured at 60 second intervals. In this particular simulation, the transition matrix $\mathbf{W}$ has no time delay and the reference site is offset from the remote by 25 km. Introducing a transition matrix with no time delay, results in transformed angle corrections with minimum error. For this reason, the results shown in Figure 12 are the baseline and the EKF estimation is expected to have the minimum error when compared to estimation including time

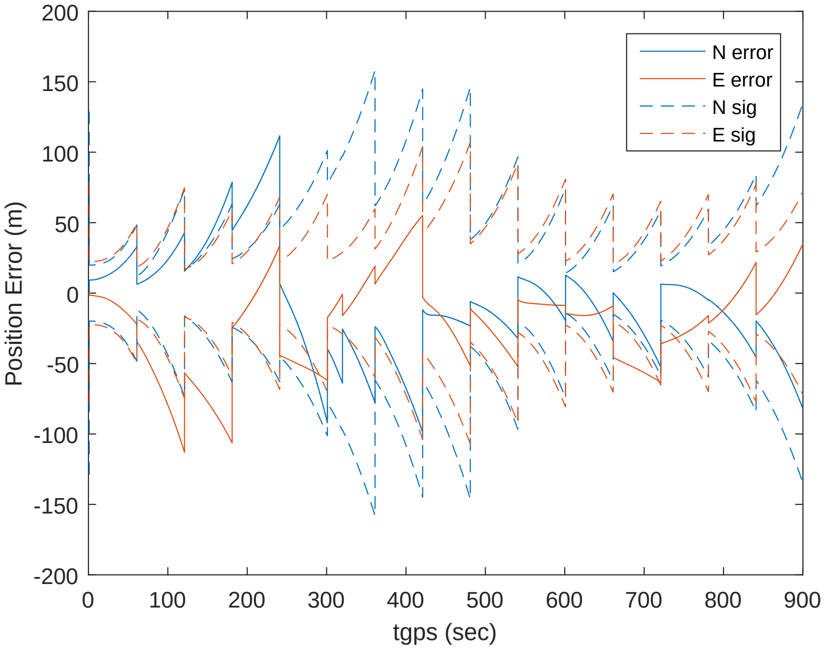

Figure 12. EKF North (blue) and East (red) position estimate errors with baro, 1 Hz star tracker angle updates and 60s ephemeris correction from reference site. Reference site separated by 25 km with remote and no time delay. Dotted lines denote 2-σ variances in each direction.

delays. The DRMS error for this particular simulation, is approximately 55 m. When we compared these results to the error previously obtained when integrating angles only measurements without the bias update, the DRMS error was reduced by 98%. This reduction in the DRMS error showed a significant improvement in the estimate of the navigation solution, when incorporating the star tracker measurements and the ephemeris correction from the reference site.

However, due to the behavior previously observed in Figure 5, interest was placed in tracking the behavior of the bias state, as it appears to be dynamic and increasing in magnitude as the baseline distance is increased. The next section analyzes the filter estimation of these bias states.

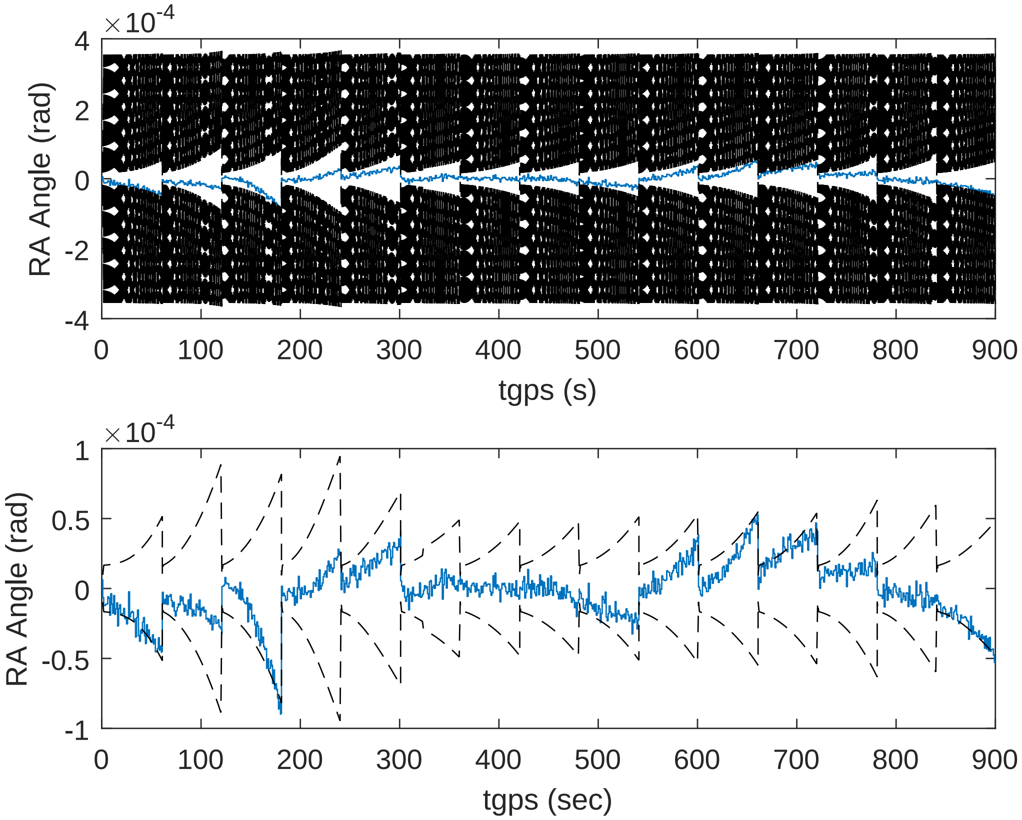

Figure 13. Right ascension bias estimate (blue) with 60 second ephemeris correction updates with noiseless TLE. Dotted lines denote 2-σ variances.

4.4.4 EKF Bias State

As shown earlier in the previous section, the error in position was significantly reduced when adding the reference site corrections as another measurement to the EKF in addition to the pointing angles. In addition of the reduced error, it is of interest to determine if the EKF is estimating the bias, $\mathbf{b}_s$, in the measurement model presented in Equation (3.49) correctly.

To validate the dynamics and measurement models used in the EKF, simulations were conducted without any TLE propagation error and both sites co-located. By not having noise in the TLE, the only source of noise in the results are the noise introduced by the sensor. The results of this simulation are analyzed in this section by focusing

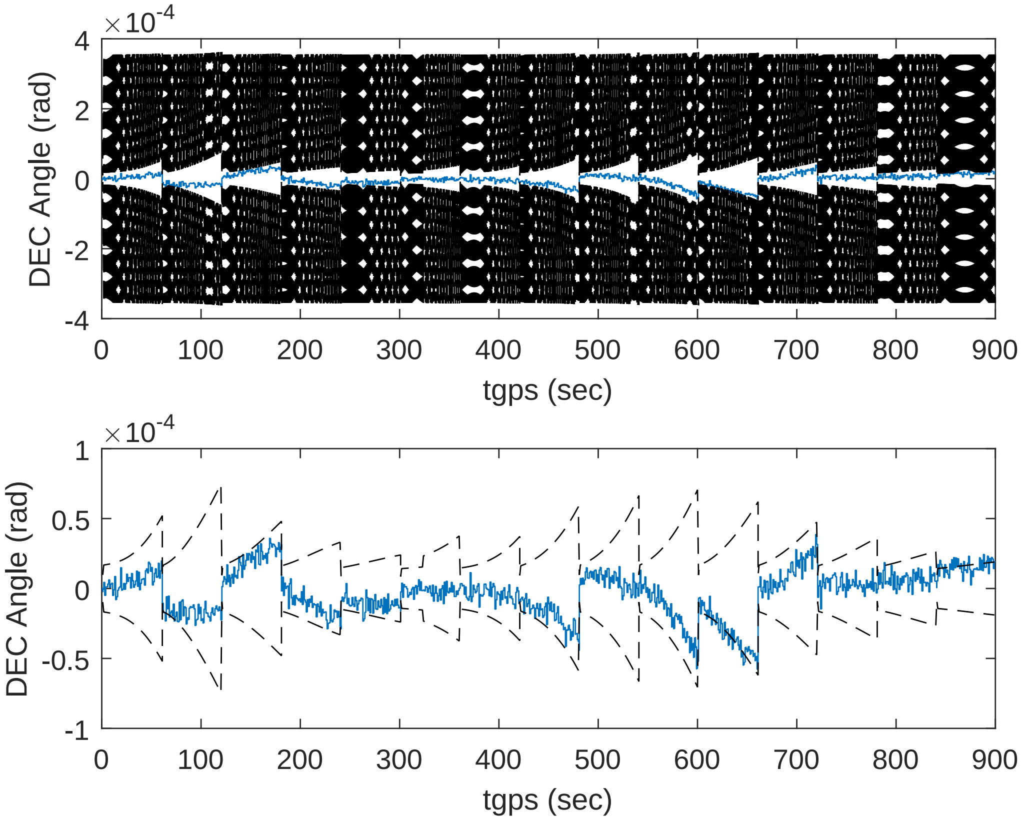

Figure 14. Declination bias estimate (blue) with 60 second ephemeris correction updates with noiseless TLE. Dotted lines denote 2-σ variances.

on the states added to the SPIDER framework. The other states in the SPIDER model have been studied and verified in previous research work [10], for this reason several simulations were run with SPIDER built in sensors to verify its performance. However, full detailed analysis was not included in this section. This section analyzes the filter's performance in estimating the added states related to the star tracker sensor, with emphasis in the satellite ephemeris bias states. The results depicting the state estimates for the bias in the right ascension with no ephemeris error is shown in Figure 13 and in declination shown in Figure 14. The subplots shown in Figures 13 and 14 is the same data but represented differently. In the top plots the covariance has a wide bound which is constantly changing. The covariance value is constantly changing from the maximum which in part is driven by the noise strength specified in the dynamics model, given by Equation (3.55). Using the parameters previously specified the theoretical value for the maximum value of the covariance is $4.8 \times 10^{-}4$ and the value obtained in the simulation was $3.55 \times 10^{-}4$. This value is updated every second indirectly by the $\mathbf{H}_{st1}$ as defined in Equation (3.66a) which relate the measured angles from the remote site to the states. Some information regarding the bias states is in this measurement update. For this reason the covariance is driven down with each measurement because the covariance of the sensor is 1 arc second. However, the direct measurement for that bias state is integrated by the EKF every 60 seconds. As depicted in Figures 13 and 14, the covariance is properly updated every 60 seconds. In addition to the covariance propagation and update of the bias state, on average the state estimate is bounded by the covariance. Based on these results we validated the star tracker models used for the system dynamics and measurements when the two sites are co-located. Additionally, the DRMS achieved, of 39 m, is the lowest value achieved in the scenarios simulated. To clearly show these results on the bias states, the bottom plot of Figures 13 and 14 are the a posteriori value of the covariance.

With noise introduced again to the TLE and with a separation distance of 100 km between the reference site and remote site, Figure 15 shows the filter estimate of the RA and DEC bias states. At distances of 100 km an greater the filter bias states starts to become overconfident, and during periods of times the state estimates are outside the covariance bounds, as depicted in Figure 15. This degradation of the filter estimation of the bias states continues for larger baseline distances. This degradation of the filter estimates was related to the increase in DRMS error for the same large distances.

Attempting to improve the estimation of the bias states, a scaling factor was applied to the noise strength of the measurement of the bias state $\mathbf{R}_{st2}$ for a distance

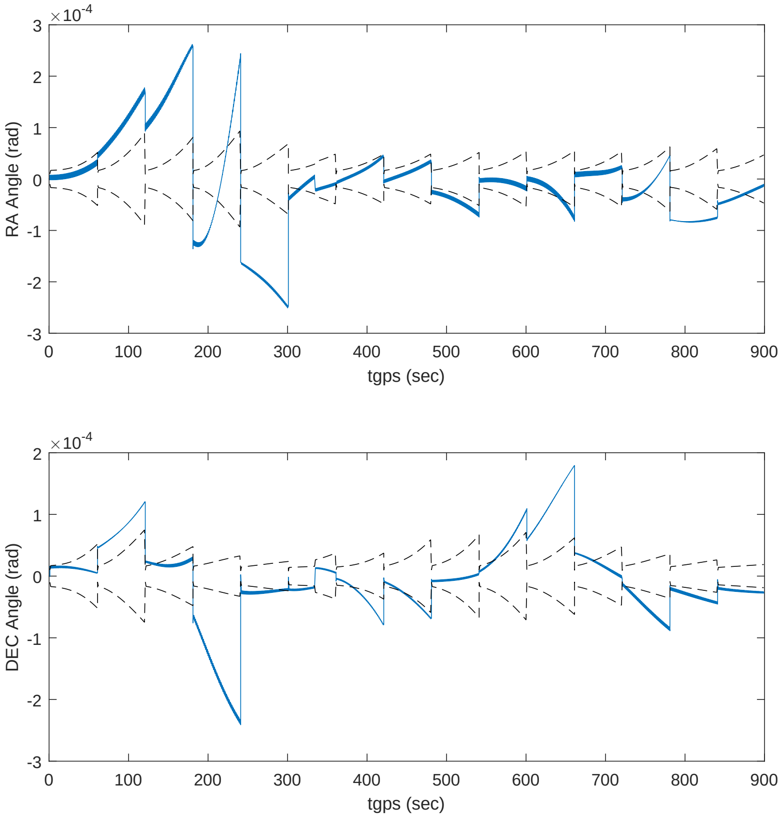

Figure 15. Satellite bias state RA(top) and DEC(bottom) when reference site and remote are separated by 100 km. Estimate (blue) and state variance (2-σ, black).

of 500 km, with the objective of reducing the DRMS error. The reason for this scale factor was due to the linear residual growth discussed in Section 4.3 and depicted in Figure 8, in an attempt to bound the state estimates by the increased covariance. Preliminary results of a particular simulation show a reduction of DRMS error at a distance of 500 km, from 1276 m with no scaling depicted in Figure 16, to 553 m with a scale factor of 1×10^3 depicted in Figure 17.

4.5 Position Error

Section 4.4 showed results and discussed DRMS values for specific scenarios. This section will combine those results under a variety of conditions into one chart that

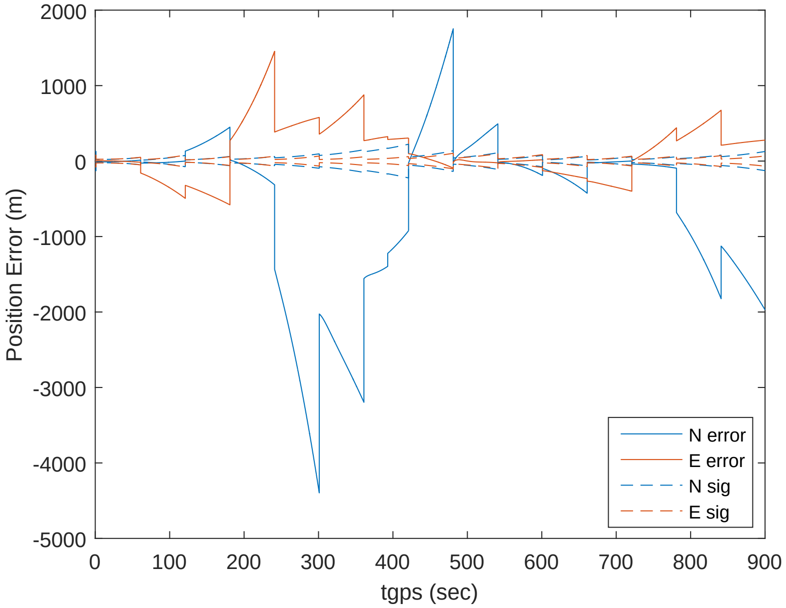

Figure 16. EKF North (blue) and East (red) position estimate errors with baro and 1 Hz star tracker angle updates and ephemeris updates without scaling factor. Dotted lines denote 2-σ variances in each direction.

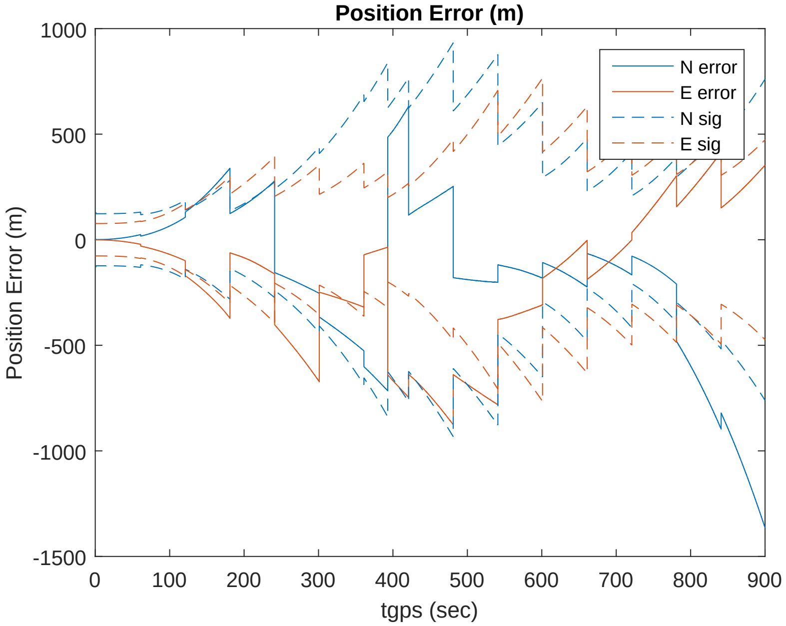

Figure 17. EKF North (blue) and East (red) position estimate errors with baro and 1 Hz star tracker angle updates and ephemeris updates with scaling factor of 1×10^3. Dotted lines denote 2-σ variances in each direction.

depicts how the DRMS is affected by distance and time delays in Figure 18. Multiple simulations were completed at each distance from 0 to 2000 km, along several heading angles 0 to 2π, with time delays ranging from 0 to 30 seconds. The DRMS error was calculated from the output of the EKF for each of those simulations, then averaged along the heading angle for that distance and time delay.

From the results obtained and shown in Figure 18, distances under 200 km the DRMS values are under 500 m and may be of used in some navigation applications. The DRMS error up to that distance appears to be growing linearly. The effects of time delays in the DRMS error are greater at closer distances. For distances greater than 300 km the effects of time delays are negligible. At that point the DRMS error is over 1 km.

At 400 km there is a noticeable spike in the DRMS in particular for time delays of 15 seconds and 30 seconds. At those large distances the geometry is significantly different between the two sites and the transformation may not be projecting the angle corrections properly, in addition at those large distances the filter bias state estimates starts to degrade. Since Figure 18 is the average DRMS, and heading angle relative to the reference affects the transformation residual, several of those simulations may have affected the averages due to poor error observability caused by satellite geometry and producing that spike.

4.6 Summary

This chapter reviewed the results of calculating the transition matrix under varying conditions and the impact in the navigation state calculated by the EKF. The parameters varied include the distances between the reference and remote site, as well as the time between when the angle bias measurement was made and applied to the angles transformed. As expected, the results showed that the closer the two

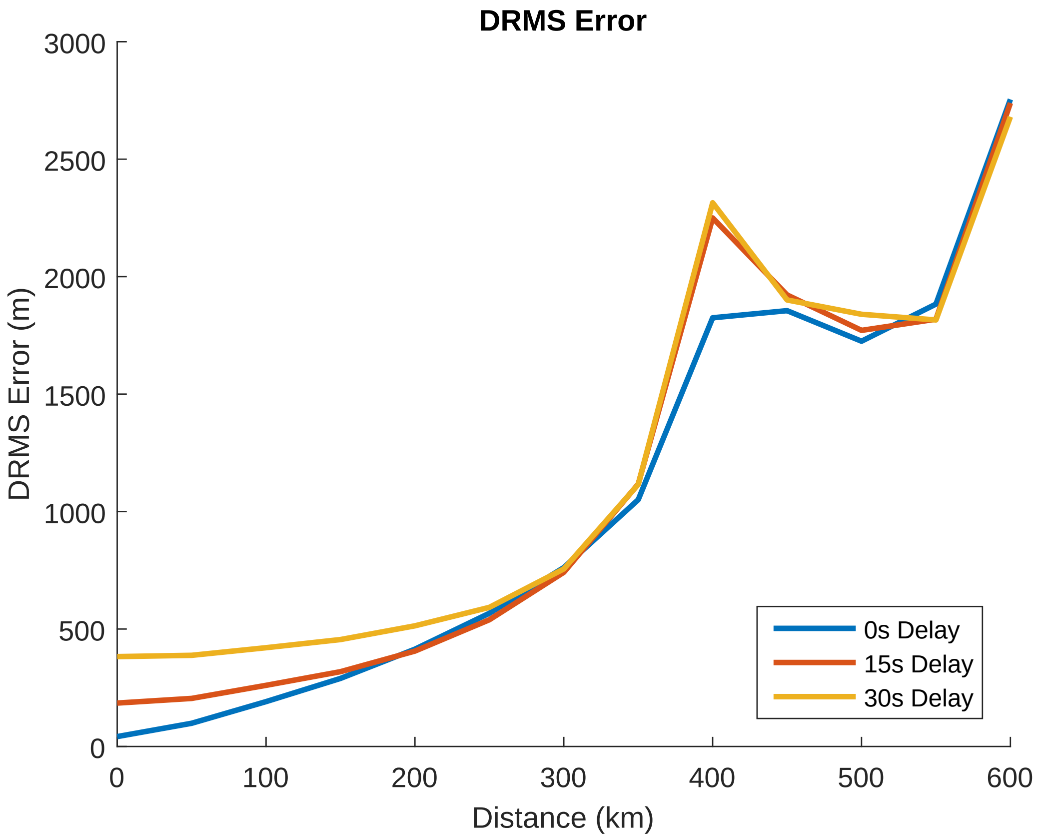

Figure 18. Average DRMS error as calculated from the EKF navigation solution for distances up to 600km and time delays from 0s to 30s.

sites are and the shorter the time delay, the transformation matrix more accurately transformed the angles. As a result, more accurate transition matrices reduced the EKF position estimate error.

Finally, the combination of increasing distance as well as time delay were simulated. These results show how both distance and time delay have a direct negative effect in the accuracy of the transformation matrix. These results are depicted in Figure 18 and provide the expected DRMS error according to the distance separation and time delay, based on the system model presented in this thesis.

Chapter V contains conclusions drawn from this research, further research that can be done to improve this correction method for obtaining better results, as well as identifying possible applications where this method could be of benefit.

V. Conclusion

5.1 Introduction

A summary of the document and the analysis of our work are discussed in this chapter. The contributions made to the body of knowledge in the field of star tracker navigation are presented. Lastly, several remarks regarding areas of further research are given as well as possible applications.

5.2 Summary of Document

Chapter I introduced the motivation for this research, the research objectives and the structure of this document. Chapter II described the current approaches to using star tracker for positioning, including using satellite observations as navigational aids. Additionally, Chapter II also presented background subject matter regarding reference frames, a technique for correcting satellite ephemeris error, and estimation using a Kalman filter. Chapter III detailed the simulation setup and approach used to analyze the data in this research. Chapter III presented the integration of the IMU, barometric altimeter, and star tracker in the EKF framework. It developed the model for the star tracker dynamics and measurements. Results are presented in Chapter IV, which include the effects of distance and time delays in the transformation matrix $\mathbf{W}$ and the position error estimated by the EKF. A mathematical method of projecting observed angles from one location to another was analyzed using simulated data and scenarios.

The simulated data supported the mathematical model, and provided insight on how that projection degraded with distance and time delays. For distances greater than 300 km, different time delays have less impact on DRMS error. At distances smaller than 300 km, those same time delays result in greater estimated position error.

A degradation of the transformation matrix with distance translates to a dynamic variance of the sensor receiving the bias update and it is not a fixed value when using the model presented in this paper. The results of estimating the bias as a FOGM process show it to be a poor approximation of the true bias state. A simple scaling method of increasing the covariance of that bias state, resulted in improved estimation of the bias, however for the limited simulations attempted the DRMS error was increased by using this method for relatively close distance (25 km) but reducing the error for larger distances (500 km). In most navigation applications, minimizing DRMS error is desirable. Therefore, with the results obtained and presented in this paper, separation distances used should be less than 200 km to obtain DRMS error under 500 m.

5.3 Summary of Contributions

The work presented in this paper provides a method of correcting for ephemeris error, when precise ephemerides are not available for the RSO observed and improve the performance of the navigation states. The measurement model for the star tracker was derived in previous work, but the derivation presented in detail in Appendix A takes into account the quadrant for the angles which is important when linearizing the measurement equations.

A method of correcting for satellite ephemeris error from a reference site by measuring angle difference which was previously proposed, was analyzed and validated in this research. A framework for incorporating satellite ephemeris corrections in the form of angles from another site was analyzed and it showed improvement in the navigation solution when using simulated data.

The results obtained in this research showed the angle bias states are not properly modeled by a FOGM. Using a FOGM for the angle measurement bias performs well for relatively close distances, but as the residual in the transformed angles grows the FOGM does not properly estimate the biases.

5.4 Future Work

During the course of this research it was identified that several aspects could be further investigated and elements of this performance model improved. First, further research in modeling the ephemeris bias state should be explored. It was shown how the transformation matrix residual increases with larger baseline distances, this limits the ability of the FOGM to correctly estimate the bias in association with the ephemeris error. A refinement in the dynamics model of these bias angles should provide significant improvement in the filter navigation solution. Applying a scaling factor to the measurement noise as the distance is increased was proposed and preliminary tested in this research. This method might be a viable alternative for improving the performance for distances over 100 km, when using the model presented in this thesis. Applying this scaling method should be explored further as well as a different bias dynamic model that can track the bias more efficiently without the filter being overconfident. In addition a backward-smoothing algorithm may also improve the estimates of the bias states, and should be explored.

Additionally, the error in the TLE was restricted by a constant bias of $\pm 0.005°$ in the inclination and the right ascending node. Therefore, the results obtained in this work are limited to this very specific type of error. To further analyze the performance of the transformation matrix different types of errors should be explored. An alternative can be introducing random Gaussian error with a standard deviation of $\pm 0.005°$ to the same parameters of the TLE. Performing the analysis on a broader set of errors helps in determining a generalized performance of the transformation matrix, consequently the performance of the filter estimation.

In addition to the varying the error introduced in the TLE, converting the observed angles from topocentric RA and DEC to other frames might provide insight on how the position error is actually represented and how it is propagating. Converting RA and DEC angle differences to cross-track and along-track error might improve categorizing the error. However, observability on these errors is also highly dependent on the geometry. At low elevations the along-track errors are difficult to resolve, and when directly above, cross-track errors tend to dominate [25].

The observations of passing satellites were made from only one reference site. A second area to further investigate is whether improvement in the accuracy of the transformation matrix could be obtained by adding a second site. Having observations from two distinct separate sites, could result in improved overall observability of the errors. This increase in observability potentially will result in improved navigation solution. Additionally, including a second reference site will provide information on the error on all three axis and improve the satellite's position measurement, which could be use for orbit estimation.

Finally, the setup chosen for this work establishes the reference site as being at different physical location from the remote. However, this same approach could be used to represent a system equipped with GNSS, that gets intermittent or partial updates. For example, if positioning via GNSS is available to the remote, it can correct for the bias state itself. This should improve the DRMS error because it has GNSS positioning for a period of time and all ephemeris error can be corrected except the measurement noise.

Appendix A. Star Tracker Angle Measurement Linearization

The measurement model presented in Equation (3.65) was linearized around a nominal value by taking the Jacobian as depicted in Equation (3.66a) in order to be applied in the EKF algorithm. The linearized simplified solution was shown in Equation (3.66b). The complete derivation is shown here. The non-linear measurements are given by Equation (3.65), also shown here.

$$\mathbf{h}_{st1}(t_i) = \begin{bmatrix} \alpha \\ \delta \end{bmatrix} = \begin{bmatrix} \tan^{-1}\left(\dfrac{P_y}{P_x}\right) \\ \sin^{-1}\left(\dfrac{P_z}{\rho}\right) \end{bmatrix} \tag{A.1}$$

where, **P** is the pointing vector from the observer to the RSO with P_x, P_y and P_z components in ECEF frame and ρ is the slant range from observer to RSO.

$$\mathbf{P} = \begin{bmatrix} P_x \\ P_y \\ P_z \end{bmatrix} = \begin{bmatrix} x_s - x_o \\ y_s - y_o \\ z_s - z_o \end{bmatrix} \tag{A.2}$$

$$\rho = \sqrt{P_x^2 + P_y^2 + P_z^2} \tag{A.3}$$

The observer's position is given in geodetic latitude, longitude and altitude (L,l,h), with units of radians, radians and meters, respectively. These geodetic coordinates are converted to ECEF by [25]

$$\mathbf{x}_o^{ecef} = \mathbf{f}(\mathbf{x}_o^n) = \begin{bmatrix} x \\ y \\ z \end{bmatrix} = \begin{bmatrix} R\cos(l) \\ R\sin(l) \\ (C_\oplus(1-e^2)+h)\sin(L) \end{bmatrix} \tag{A.4}$$

where the observer's state in the navigation frame, $\mathbf{x}_o^n$, and the coefficient R and $C_\oplus$

are given by Equations (A.5) to (A.7) [25].

$$\mathbf{x}_o^n = [L \;\; l \;\; h]^T \tag{A.5}$$

$$C_\oplus = R_E = \frac{R_\oplus}{\sqrt{1 - e^2 \sin^2 L}} \tag{A.6}$$

$$R = (C_\oplus + h)\cos(L) \tag{A.7}$$

with $R_\oplus$ and e describing the equatorial radius and the Earth's eccentricity, respectively.

Taking the Jacobian of the star tracker angle measurement model, the linearized measurement model matrix becomes

$$\mathbf{H}_{st1}(t_{i+1}) \triangleq \left. \frac{\partial \mathbf{h}_{st1}(\delta \mathbf{x}, t)}{\partial \delta \mathbf{x}(t)} \right|_{\delta \mathbf{x} = \widehat{\mathbf{x}}(t_{i+1}^-)} \tag{A.8a}$$

$$= \begin{pmatrix} \frac{\partial \alpha}{\partial \delta L} & \frac{\partial \alpha}{\partial \delta l} & \frac{\partial \alpha}{\partial \delta h} & \mathbf{0}_{1\times 12} & 1 & 0 & 0 \\ \frac{\partial \delta}{\partial \delta L} & \frac{\partial \delta}{\partial \delta l} & \frac{\partial \delta}{\partial \delta h} & \mathbf{0}_{1\times 12} & 0 & 1 & 0 \end{pmatrix} \tag{A.8b}$$

Each element of the **H** matrix are described and derived here. To retain the quadrant information when linearizing $\mathbf{h}_{st1}$, arctan was treated as a function of two variables, in this case P_y and P_x. Treating the trigonometric function as a function of two variables result in two partial derivatives, retaining information about the quadrant. This approach of treating arctan as a function of two variable is equivalent of using atan2 in computer language. Therefore, when implementing this measurement model in MATLAB®the atan2 function was used. To emphasize this difference atan2 was used in the notation.

First, the partial derivatives with respect to the 18 state vector are shown below.

$$\frac{\partial \alpha}{\partial \delta L} = \frac{\partial}{\partial \delta L}\left(atan2\left(\frac{P_y}{P_x}\right)\right) \tag{A.9a}$$

$$= \frac{\partial}{\partial P_x}\left(\tan^{-1}\left(\frac{P_y}{P_x}\right)\right)\frac{\partial P_x}{\partial \delta L} + \frac{\partial}{\partial P_y}\left(\tan^{-1}\left(\frac{P_y}{P_x}\right)\right)\frac{\partial P_y}{\partial \delta L} \tag{A.9b}$$

$$= \frac{-P_y}{P_x^2 + P_y^2}\ \frac{\partial P_x}{\partial \delta L} + \frac{P_x}{P_x^2 + P_y^2}\ \frac{\partial P_y}{\partial \delta L} \tag{A.9c}$$

$$\frac{\partial \alpha}{\partial \delta l} = \frac{\partial}{\partial \delta l}\left(atan2\left(\frac{P_y}{P_x}\right)\right) \tag{A.10a}$$

$$= \frac{\partial}{\partial P_x}\left(\tan^{-1}\left(\frac{P_y}{P_x}\right)\right)\frac{\partial P_x}{\partial \delta l} + \frac{\partial}{\partial P_y}\left(\tan^{-1}\left(\frac{P_y}{P_x}\right)\right)\frac{\partial P_y}{\partial \delta l} \tag{A.10b}$$

$$= \frac{-P_y}{P_x^2 + P_y^2}\ \frac{\partial P_x}{\partial \delta l} + \frac{P_x}{P_x^2 + P_y^2}\ \frac{\partial P_y}{\partial \delta l} \tag{A.10c}$$

$$\frac{\partial \alpha}{\partial \delta h} = \frac{\partial}{\partial \delta h}\left(atan2\left(\frac{P_y}{P_x}\right)\right) \tag{A.11a}$$

$$= \frac{\partial}{\partial P_x}\left(\tan^{-1}\left(\frac{P_y}{P_x}\right)\right)\frac{\partial P_x}{\partial \delta h} + \frac{\partial}{\partial P_y}\left(\tan^{-1}\left(\frac{P_y}{P_x}\right)\right)\frac{\partial P_y}{\partial \delta h} \tag{A.11b}$$

$$= \frac{-P_y}{P_x^2 + P_y^2}\ \frac{\partial P_x}{\partial \delta h} + \frac{P_x}{P_x^2 + P_y^2}\ \frac{\partial P_y}{\partial \delta h} \tag{A.11c}$$

$$
\begin{aligned}
\frac{\partial \delta}{\partial \delta L} &= \frac{\partial}{\partial \delta L}\left(\sin^{-1}\left(\frac{P_z}{\rho}\right)\right) && \text{(A.12a)}\\
&= \frac{1}{\sqrt{1-\left(\frac{P_z}{\rho}\right)^2}}\frac{\partial}{\partial \delta L}\left(\frac{P_z}{\rho}\right) && \text{(A.12b)}\\
&= \frac{1}{\sqrt{1-\left(\frac{P_z}{\rho}\right)^2}}\left(\frac{\rho\frac{\partial P_z}{\partial \delta L}-P_y\frac{\partial \rho}{\partial \delta L}}{\rho^2}\right) && \text{(A.12c)}
\end{aligned}
$$

$$
\begin{aligned}
\frac{\partial \delta}{\partial \delta l} &= \frac{\partial}{\partial \delta l}\left(\sin^{-1}\left(\frac{P_z}{\rho}\right)\right) && \text{(A.13a)}\\
&= \frac{1}{\sqrt{1-\left(\frac{P_z}{\rho}\right)^2}}\frac{\partial}{\partial \delta l}\left(\frac{P_z}{\rho}\right) && \text{(A.13b)}\\
&= \frac{1}{\sqrt{1-\left(\frac{P_z}{\rho}\right)^2}}\left(\frac{\rho\cancelto{0}{\frac{\partial P_z}{\partial \delta l}}-P_y\frac{\partial \rho}{\partial \delta l}}{\rho^2}\right) && \text{(A.13c)}\\
&= \frac{1}{\sqrt{1-\left(\frac{P_z}{\rho}\right)^2}}\left(\frac{-P_y\frac{\partial \rho}{\partial \delta l}}{\rho^2}\right) && \text{(A.13d)}
\end{aligned}
$$

$$\frac{\partial \delta}{\partial \delta h} = \frac{\partial}{\partial \delta h}\left(\sin^{-1}\left(\frac{P_z}{\rho}\right)\right) \tag{A.14a}$$

$$= \frac{1}{\sqrt{1-\left(\frac{P_z}{\rho}\right)^2}}\frac{\partial}{\partial \delta h}\left(\frac{P_z}{\rho}\right) \tag{A.14b}$$

$$= \frac{1}{\sqrt{1-\left(\frac{P_z}{\rho}\right)^2}}\left(\frac{\rho\frac{\partial P_z}{\partial \delta h} - P_y\frac{\partial \rho}{\partial \delta h}}{\rho^2}\right) \tag{A.14c}$$

$$= \frac{1}{\sqrt{1-\left(\frac{P_z}{\rho}\right)^2}}\left(\frac{-\rho\sin(L) - P_y\frac{\partial \rho}{\partial \delta h}}{\rho^2}\right) \tag{A.14d}$$

Next the partial derivatives needed to completely solve the partials with respect to the state vector presented earlier, are derived below. These are the partial derivatives of the pointing vector from the observer to the satellite.

$$\begin{aligned}
\frac{\partial P_x}{\partial \delta L} &= \frac{\partial}{\partial \delta L}(x_s - x_o) && \text{(A.15a)}\\
&= 0 - \frac{\partial x_o}{\partial \delta L} && \text{(A.15b)}\\
&= -\frac{\partial}{\partial \delta L}(R\cos(l+\delta l)) && \text{(A.15c)}\\
&= -\cos(l+\delta l)\frac{\partial R}{\partial \delta L} - R\cancelto{0}{\frac{\partial}{\partial \delta L}\cos(l+\delta l)} && \text{(A.15d)}\\
&= -\cos(l+\delta l)\frac{\partial R}{\partial \delta L} && \text{(A.15e)}\\
&= -\cos(l+\delta l)\left[\cos(L+\delta L)\frac{R_\oplus e^2\cos(L+\delta L)\sin(L+\delta L)}{(1-e^2 sin^2(L+\delta L))^{3/2}} - \sin(L+\delta L)(C_\oplus + h)\right] && \\
& && \text{(A.15f)}\\
&= \cos(l+\delta l)\sin(L+\delta L)(C_\oplus + h) - \frac{R_\oplus e^2\cos^2(L+\delta L)\cos(l+\delta l)\sin(L+\delta L)}{(1-e^2 sin^2(L+\delta L))^{3/2}} && \\
& && \text{(A.15g)}
\end{aligned}$$

$$\begin{aligned}
\frac{\partial P_x}{\partial \delta l} &= \frac{\partial}{\partial \delta l}(x_s - x_o) && \text{(A.16a)}\\
&= 0 - \frac{\partial x_o}{\partial \delta l} && \text{(A.16b)}\\
&= -\frac{\partial}{\partial \delta l}(R\cos(l+\delta l)) && \text{(A.16c)}\\
&= -\cos(l+\delta l)\cancelto{0}{\frac{\partial R}{\partial \delta l}} - R\frac{\partial}{\partial \delta l}\cos(l+\delta l) && \text{(A.16d)}\\
&= R\sin(l+\delta l) && \text{(A.16e)}
\end{aligned}$$

$$\frac{\partial P_x}{\partial \delta h} = \frac{\partial}{\partial \delta h}(x_s - x_o) \tag{A.17a}$$

$$= 0 - \frac{\partial x_o}{\partial \delta h} \tag{A.17b}$$

$$= -\frac{\partial}{\partial \delta h}(R\cos(l + \delta l)) \tag{A.17c}$$

$$= -\cos(l + \delta l)\frac{\partial R}{\partial \delta h} - R\frac{\partial}{\partial \delta h}\cos(l + \delta l) \tag{A.17d}$$

$$= -\cos(l + \delta l)\cos(L + \delta L) \tag{A.17e}$$

$$\frac{\partial P_y}{\partial \delta L} = \frac{\partial}{\partial \delta L}(y_s - y_o) \tag{A.18a}$$

$$= 0 - \frac{\partial y_o}{\partial \delta L} \tag{A.18b}$$

$$= -\frac{\partial}{\partial \delta L}(R\sin(l + \delta l)) \tag{A.18c}$$

$$= -\sin(l + \delta l)\frac{\partial R}{\partial \delta L} - R\frac{\partial}{\partial \delta L}\sin(l + \delta l) \tag{A.18d}$$

$$= -\sin(l + \delta l)\frac{\partial R}{\partial \delta L} - 0 \tag{A.18e}$$

$$= -\sin(l + \delta l)\left[\cos(L + \delta L)\frac{R_\oplus e^2 \cos(L + \delta L)\sin(L + \delta L)}{(1 - e^2 sin^2(L + \delta L))^{3/2}} - \sin(L + \delta L)(C_\oplus + h)\right] \tag{A.18f}$$

$$= \sin(l + \delta l)\sin(L + \delta L)(C_\oplus + h) - \frac{R_\oplus e^2 \cos^2(L + \delta L)\sin(l + \delta l)\sin(L + \delta L)}{(1 - e^2 sin^2(L + \delta L))^{3/2}} \tag{A.18g}$$

$$\frac{\partial P_y}{\partial \delta l} = \frac{\partial}{\partial \delta l}(y_s - y_o) \tag{A.19a}$$

$$= 0 - \frac{\partial y_o}{\partial \delta l} \tag{A.19b}$$

$$= -\frac{\partial}{\partial \delta l}(R \sin(l + \delta l)) \tag{A.19c}$$

$$= -\sin(l + \delta l)\cancelto{0}{\frac{\partial R}{\partial \delta l}} - R\frac{\partial}{\partial \delta l}\sin(l + \delta l) \tag{A.19d}$$

$$= -R\cos(l + \delta l) \tag{A.19e}$$

$$\frac{\partial P_y}{\partial \delta h} = \frac{\partial}{\partial \delta h}(y_s - y_o) \tag{A.20a}$$

$$= 0 - \frac{\partial y_o}{\partial \delta h} \tag{A.20b}$$

$$= -\frac{\partial}{\partial \delta h}(R \sin(l + \delta l)) \tag{A.20c}$$

$$= -\sin(l + \delta l)\frac{\partial R}{\partial \delta h} - R\cancelto{0}{\frac{\partial}{\partial \delta h}\sin(l + \delta l)} \tag{A.20d}$$

$$= -\sin(l + \delta l)\cos(L + \delta L) \tag{A.20e}$$

$$\frac{\partial P_z}{\partial L} = \frac{\partial}{\partial \delta L}(z_s - z_o) \tag{A.21a}$$

$$= 0 - \frac{\partial z_o}{\partial \delta L} \tag{A.21b}$$

$$= -\frac{\partial}{\partial \delta L}(((C_\oplus(1-e^2)) + h)\sin(l + \delta l)) \tag{A.21c}$$

$$= -(1-e^2)\sin(L+\delta L)\frac{\partial C_\oplus}{\partial \delta L} - \cos(L+\delta L)(C_\oplus(1-e^2) + h + \delta h) \tag{A.21d}$$

$$\begin{aligned} &= -(1-e^2)\sin(L+\delta L)\frac{R_\oplus e^2 \cos(L+\delta L)\sin(L+\delta L)}{(1-e^2 sin^2(L+\delta L))^{3/2}} - \\ &\quad \cos(L+\delta L)(C_\oplus(1-e^2) + h + \delta h) \end{aligned} \tag{A.21e}$$

$$\frac{\partial P_z}{\partial \delta l} = \frac{\partial}{\partial \delta l}(z_s - z_o) \tag{A.22a}$$

$$= 0 - \frac{\partial z_o}{\partial \delta l} \tag{A.22b}$$

$$= -\frac{\partial}{\partial \delta l}(((C_\oplus(1-e^2)) + h + \delta h)\sin(l + \delta l)) \tag{A.22c}$$

$$= -(1-e^2)\sin(L)\cancelto{0}{\frac{\partial C_\oplus}{\partial \delta l}} - (C_\oplus(1-e^2) + h + \delta h)\cancelto{0}{\frac{\partial \sin(L+\delta L)}{\partial \delta l}} \tag{A.22d}$$

$$= 0 - 0 = 0 \tag{A.22e}$$

$$\frac{\partial P_z}{\partial \delta h} = \frac{\partial}{\partial \delta h}(z_s - z_o) \tag{A.23a}$$

$$= 0 - \frac{\partial z_o}{\partial \delta h} \tag{A.23b}$$

$$= -\frac{\partial}{\partial \delta h}(((C_\oplus(1-e^2)) + h + \delta h)\sin(l + \delta l)) \tag{A.23c}$$

$$= -\left[(1-e^2)\cancelto{0}{\frac{\partial C_\oplus}{\partial \delta h}} + 1\right]\sin(L+\delta L) - (C_\oplus(1-e^2) + h + \delta h)\cancelto{0}{\frac{\partial \sin(L+\delta L)}{\partial \delta h}} \tag{A.23d}$$

$$= -\sin(L+\delta L) \tag{A.23e}$$

Below, the partial derivatives of the slant range with respect to the states.

$$\frac{\partial \rho}{\partial L} = \frac{\partial}{\partial \delta L}\sqrt{P_x^2 + P_y^2 + P_z^2} \tag{A.24a}$$

$$= \frac{1}{2\rho}\frac{\partial}{\partial \delta L}(P_x^2 + P_y^2 + P_z^2) \tag{A.24b}$$

$$= \frac{1}{2\rho}\left[2P_x\frac{\partial P_x}{\partial \delta L} + 2P_y\frac{\partial P_y}{\partial \delta L} + 2P_z\frac{\partial P_z}{\partial \delta L}\right] \tag{A.24c}$$

$$= \frac{1}{\rho}\left[P_x\frac{\partial P_x}{\partial \delta L} + P_y\frac{\partial P_y}{\partial \delta L} + P_z\frac{\partial P_z}{\partial \delta L}\right] \tag{A.24d}$$

$$\begin{aligned} = \frac{1}{\rho}\Bigg[&P_x\Bigg(\cos(l+\delta l)\sin(L+\delta L)(C_\oplus + h + \delta h) - \\ &\qquad \frac{R_\oplus e^2\cos^2(L+\delta L)\cos(l+\delta l)\sin(L+\delta L)}{(1-e^2sin^2(L+\delta L))^{3/2}}\Bigg) + \\ &P_y\Bigg(\sin(l+\delta l)\sin(L+\delta L)(C_\oplus + h + \delta h) - \\ &\qquad \frac{R_\oplus e^2\cos^2(L+\delta L)\sin(l+\delta l)\sin(L+\delta L)}{(1-e^2sin^2(L+\delta L))^{3/2}}\Bigg) + \\ &P_z\Bigg(-(1-e^2)\sin(L+\delta L)\frac{R_\oplus e^2\cos(L+\delta L)\sin(L+\delta L)}{(1-e^2sin^2(L+\delta L))^{3/2}} - \\ &\qquad \cos(L+\delta L)(C_\oplus(1-e^2) + h + \delta h)\Bigg)\Bigg] \end{aligned} \tag{A.24e}$$

$$\frac{\partial \rho}{\partial \delta l} = \frac{\partial}{\partial \delta l}\sqrt{P_x^2 + P_y^2 + P_z^2} \tag{A.25a}$$

$$= \frac{1}{2\rho}\frac{\partial}{\partial \delta l}(P_x^2 + P_y^2 + P_z^2) \tag{A.25b}$$

$$= \frac{1}{2\rho}\left[2P_x\frac{\partial P_x}{\partial \delta l} + 2P_y\frac{\partial P_y}{\partial \delta l} + 2P_z\frac{\partial P_z}{\partial \delta l}\right] \tag{A.25c}$$

$$= \frac{1}{\rho}\left[P_x\frac{\partial P_x}{\partial \delta l} + P_y\frac{\partial P_y}{\partial \delta l} + P_z\cancelto{0}{\frac{\partial P_z}{\partial \delta l}}\right] \tag{A.25d}$$

$$= \frac{1}{\rho}\left[P_x\left(R\sin(L + \delta L)\right) + P_y\left(-R\cos(l + \delta l)\right)\right] \tag{A.25e}$$

$$\frac{\partial \rho}{\partial \delta h} = \frac{\partial}{\partial \delta h}\sqrt{P_x^2 + P_y^2 + P_z^2} \tag{A.26a}$$

$$= \frac{1}{2\rho}\frac{\partial}{\partial \delta h}(P_x^2 + P_y^2 + P_z^2) \tag{A.26b}$$

$$= \frac{1}{2\rho}\left[2P_x\frac{\partial P_x}{\partial \delta h} + 2P_y\frac{\partial P_y}{\partial \delta h} + 2P_z\frac{\partial P_z}{\partial \delta h}\right] \tag{A.26c}$$

$$= \frac{1}{\rho}\left[P_x\frac{\partial P_x}{\partial \delta h} + P_y\frac{\partial P_y}{\partial \delta h} + P_z\frac{\partial P_z}{\partial \delta h}\right] \tag{A.26d}$$

$$= \frac{1}{\rho}\left[P_x\left(-\cos(l + \delta l)\cos(L + \delta L)\right) + P_y\left(-\cos(L + \delta L)\sin(l + \delta l)\right) + P_z\left(-\sin(L + \delta L)\right)\right] \tag{A.26e}$$

Finally, the partial derivatives of the ECEF conversion coefficient with respect to the error states are derived.

$$\frac{\partial C_\oplus}{\partial \delta L} = \frac{\partial}{\partial \delta L}\left(\frac{R_\oplus}{\sqrt{1-e^2\sin^2(L)}}\right) \tag{A.27a}$$

$$= 0 - \frac{R_\oplus}{2}(1-e^2\sin^2(L))^{-1/2} \quad \frac{\partial}{\partial \delta L}(1-e^2\sin^2(L)) \tag{A.27b}$$

$$= \frac{(0-\frac{R_\oplus}{2}(1-e^2\sin^2(L))^{-1/2})\ (0-2e^2\cos(L)\sin(L))}{(\sqrt{1-e^2\sin^2(L)})^2} \tag{A.27c}$$

$$= \frac{R_\oplus e^2\cos(L)\sin(L)}{(1-e^2 sin^2(L))^{3/2}} \tag{A.27d}$$

$$\frac{\partial C_\oplus}{\partial \delta l} = \frac{\partial}{\partial \delta l}\left(\frac{R_\oplus}{\sqrt{1-e^2\sin^2(L)}}\right) = 0 \tag{A.28}$$

$$\frac{\partial C_\oplus}{\partial \delta h} = \frac{\partial}{\partial \delta h}\left(\frac{R_\oplus}{\sqrt{1-e^2\sin^2(L)}}\right) = 0 \tag{A.29}$$

$$\frac{\partial R}{\partial \delta L} = \frac{\partial}{\partial \delta L}((C_\oplus + h)\cos(L)) \tag{A.30a}$$

$$= \cos(L)\frac{\partial}{\partial \delta L}(C_\oplus + h) - \sin(L)(C_\oplus + h) \tag{A.30b}$$

$$= \cos(L)\frac{R_\oplus e^2\cos(L)\sin(L)}{(1-e^2 sin^2(L))^{3/2}} - \sin(L)(C_\oplus + h) \tag{A.30c}$$

$$\frac{\partial R}{\partial l} = \frac{\partial}{\partial \delta l}((C_\oplus + h)\cos(L)) \tag{A.31a}$$

$$= \cos(L)\cancelto{0}{\frac{\partial}{\partial \delta l}(C_\oplus + h)} + (C_\oplus + h)\cancelto{0}{\frac{\partial}{\partial \delta l}\cos(L)} \tag{A.31b}$$

$$= 0 \tag{A.31c}$$

$$
\begin{aligned}
\frac{\partial R}{\partial \delta h} &= \frac{\partial}{\partial \delta h}((C_\oplus + h)\cos(L)) && \text{(A.32a)} \\
&= \cos(L)(0+1) + (C_\oplus + h)\cancelto{0}{\frac{\partial}{\partial \delta h}\cos(L)} && \text{(A.32b)} \\
&= \cos(L) && \text{(A.32c)}
\end{aligned}
$$

Combining the partial derivatives presented in this Appendix, the linearized measurement model can be implemented in the EKF filter.

Bibliography

1. Autonomy & Navigation Technology Center. *Interface Control Document for Sensor Processing and Inertial Dynamics Error Reduction (SPIDER) Program*, 2014.

2. Bellows, Capt Charlie T. *Leveraging External Sensor Data for Enhanced Space Situational Awareness*. Ph.D. thesis, AIR FORCE INSTITUTE OF TECHNOLOGY, 2015.

3. Betke, M. and L. Gurvits. "Mobile robot localization using landmarks". *IEEE Transactions on Robotics and Automation*, 13(2):251–263, April 1997. ISSN 1042296X. URL `http://ieeexplore.ieee.org/lpdocs/epic03/wrapper.htm?arnumber=563647`.

4. CelesTrak. "NORAD Two-Line Elements Sets". `http://celestrak.com/NORAD/elements/`. Accessed: 2015-08-10.

5. Control, USSTRATCOM Space and Space Surveillance. "JSpOC", 2014. URL `http://www.stratcom.mil/f11`.

6. Division, NOAA/ESRL's Global Monitoring. "Celestial Sphere", 2015. URL `http://www.esrl.noaa.gov/gmd/grad/solcalc/celsphere.gif`.

7. Hoots, Felix R., Paul W. Schumacher Jr., and Robert a. Glover. "History of Analytical Orbit Modeling in the U. S. Space Surveillance System". *Journal of Guidance, Control, and Dynamics*, 27(2):174–185, 2004. ISSN 0731-5090.

8. Kaplan, George H. "A Closed-Form Position and Velocity Solution for Angles-Only Navigation". 2006.

9. Kaplan, George H. “Angles-Only Navigation: Position and Velocity Solution from Absolute Triangulation”. *Navigation*, 58(3):187–201, 2011.
10. Kawecki, James E.C. “Initial Implementation And Testing Of A Tightly-Coupled IMU/Pseudolite System”, 2015.
11. Kervin, Paul, Vicki S Hoo, Daron Nishimoto, and Dennis Liang. *Rapidly deployable Raven-class systems SSA Support in the Field*. Technical report, DTIC Document, 2009.
12. Lang, D., D. W. Hogg, K. Mierle, M. Blanton, and S. Roweis. “Astrometry.net: Blind Astrometric Calibration of Arbitrary Astronomical Images”. 139:1782–1800, May 2010.
13. Levesque, M. “Automatic Reacquisition of Satellite Positions by Detecting Their Expected Streaks in Astronomical Images”. *Advanced Maui Optical and Space Surveillance Technologies Conference*, 81. 2009.
14. Levit, Creon and William Marshall. “Improved orbit predictions using two-line elements”. *Advances in Space Research*, 47(7):1107–1115, 2011. ISSN 02731177. URL `http://dx.doi.org/10.1016/j.asr.2010.10.017`.
15. MATLAB. *version 8.5.0.197613 (R2015a)*. The MathWorks Inc., 2015.
16. Obama, President Barack. “National Space Policy of the United States of America”, 2010. URL `https://www.whitehouse.gov/sites/default/files/national_space_policy_6-28-10.pdf`.
17. Oniga, Florin, Melania Miron, Radu Danescu, and Sergiu Nedevschi. “Automatic recognition of low earth orbit objects from image sequences”. *IEEE International Conference on Intelligent Computer Communication and Processing*. 2011.

18. Peter, S Maybeck. *Stochastic Models, Estimation, and Control. Vol. 1.* New York, NY: Academic Press, 1979.

19. Pierce, Scott J. *Modeling Navigation System Performance of a Satellite-Observing Star Tracker Tightly Integrated with an Inertial Measurement Unit.* Ph.D. thesis, Air Force Institute of Technology, 2015.

20. Schmunk, Matthew M. *Initial Determination of Low Earth Orbits Using Commercial Telescopes.* Master's thesis, Air Force Institute of Technology, 2008.

21. Sinnott, Roger. "Virtues of the Haversine". 1984.

22. Sydney, Paul F., John L. Africano, Amy Fredericks, Kris M. Hamada, Vicki SooHoo, Daron L. Nishimoto, Paul W. Kervin, Steve Bisque, and Matthew Bisque. "Raven automated small telescope systems". volume 4091, 237–247. 2000.

23. Systems Tool Kit (STK). *version 10.1.3.* Analytical Graphics, Inc. (AGI), 2014.

24. Titterton, David and John L Weston. *Strapdown inertial navigation technology*, volume 17. IET, 2004.

25. Vallado, David A and Wayne D McClain. *Fundamentals of Astrodynamics and Applications.* Kluwer Academic Publishers, 2nd edition, 2001.

REPORT DOCUMENTATION PAGE

Form Approved
OMB No. 0704–0188

1. REPORT DATE *(DD–MM–YYYY)*	**2. REPORT TYPE**	**3. DATES COVERED** *(From — To)*
24–03–2016	Master's Thesis	Sept 2014 — Mar 2016

4. TITLE AND SUBTITLE

Satellite Ephemeris Correction via Remote Site Observation for Star Tracker Navigation Performance Improvement

5a. CONTRACT NUMBER

5b. GRANT NUMBER

5c. PROGRAM ELEMENT NUMBER

6. AUTHOR(S)

Díaz, Jorge E., Capt, USAF

5d. PROJECT NUMBER

5e. TASK NUMBER

5f. WORK UNIT NUMBER

7. PERFORMING ORGANIZATION NAME(S) AND ADDRESS(ES)

Air Force Institute of Technology
Graduate School of Engineering and Management (AFIT/EN)
2950 Hobson Way
WPAFB OH 45433-7765

8. PERFORMING ORGANIZATION REPORT NUMBER

AFIT-ENG-MS-16-M-013

9. SPONSORING / MONITORING AGENCY NAME(S) AND ADDRESS(ES)

Intentionally Left Blank

10. SPONSOR/MONITOR'S ACRONYM(S)

11. SPONSOR/MONITOR'S REPORT NUMBER(S)

12. DISTRIBUTION / AVAILABILITY STATEMENT

DISTRIBUTION STATEMENT A:
APPROVED FOR PUBLIC RELEASE; DISTRIBUTION UNLIMITED.

13. SUPPLEMENTARY NOTES

This material is declared a work of the U.S. Government and is not subject to copyright protection in the United States.

14. ABSTRACT

This thesis analyzed a method to correct for satellite ephemeris to be used in celestial navigation applications. This correction is the measured angle difference between the expected location of the satellite, which is given by propagating publicly available Two-Line Element sets (TLE), and their observed angles from a precisely known reference site. Therefore, the angle difference can be attributed completely to satellite ephemeris error assuming instrument error was accounted for. The intent is to calculate this correction from the reference site and relate it to remote sites that have visibility of the same satellite, but where its own location is known with some uncertainty. The effects of increased baseline distances from the reference site are studied, as well as time delays.

15. SUBJECT TERMS

extended Kalman filter, star tracker, celestial navigation, satellite observation, ephemeris correction, image-aided navigation

16. SECURITY CLASSIFICATION OF:			**17. LIMITATION OF ABSTRACT**	**18. NUMBER OF PAGES**	**19a. NAME OF RESPONSIBLE PERSON**
a. REPORT	**b. ABSTRACT**	**c. THIS PAGE**			Maj Scott J. Pierce, AFIT/ENG
U	U	U	U	92	**19b. TELEPHONE NUMBER** *(include area code)* (937) 255-3636, x3419; scott.pierce@afit.edu

Standard Form 298 (Rev. 8–98)
Prescribed by ANSI Std. Z39.18